



High-temperature nitridation of Nb–Ti alloys in nitrogen

V. Buscaglia^{a,*}, A. Martinelli^a, R. Musenich^b, W. Mayr^c, W. Lengauer^c

^a*Institute of Physical Chemistry of Materials, National Institute for Advanced Materials and Related Applications, National Research Council, via De Marini 6, I-16149 Genoa, Italy*

^b*National Institute of Nuclear Physics, via Dodecaneso 33, I-16146 Genoa, Italy*

^c*Institute for Chemical Technology of Inorganic Materials, Vienna University of Technology, Getreidemarkt 9/161, A-1060 Vienna, Austria*

Received 13 July 1998; received in revised form 13 October 1998

Abstract

Microstructure evolution, phase composition, weight gain and layer growth kinetics of Nb–Ti alloys (10, 47, 63 and 90 at.% Ti) annealed in high-purity nitrogen atmosphere (0.3, 3 and 30 bar) were studied in the temperature range 1300–1600°C. After nitridation, the formation of an external compact nitride layer as well as extensive internal nitride precipitation was observed. The overall nitridation kinetics (weight gain) is invariably parabolic; a deviation from the initial rate law is observed at 1450 and 1600°C for the longer reaction times when the alloy core approaches nitrogen saturation and internal precipitation slows down. The parabolic rate constant is strongly affected by the Nb content in the alloy. The phases detected in the reacted samples are isostructural with those of the Nb–Ti, Nb–N and Ti–N systems. The surface nitride was δ -(Ti,Nb)N in any case. The morphology of the internal nitridation zone corresponds to the growth of large, oriented, nitride needles for the three alloys richer in titanium. The needles are composed of α -(Ti,Nb)(N) in the case of Ti₉₀Nb₁₀ alloy and of δ -(Ti,Nb)N_{1-x} in the case of Ti₆₃Nb₃₇ and Ti₄₇Nb₅₃. Such a microstructure is evidence for nucleation difficulty; coarsening of the existing particles is favoured in comparison to the formation of new precipitates. Homogeneous nucleation is hindered by the small chemical Gibbs free energy available and the elastic strain energy related to volume misfit. After initial reaction, microstructure evolution is mainly determined by the fast inward diffusion of nitrogen and the slow Nb–Ti interdiffusion in the β -(Ti,Nb) alloy. Internal nitridation of Ti₁₀Nb₉₀ at 1450 and 1600°C leads to the formation of fine and numerous precipitates of β -(Nb,Ti)₂N. In this case heterogeneous nucleation along grain boundaries and dislocation lines is the prevailing mechanism. © 1999 Elsevier Science S.A. All rights reserved.

Keywords: Nitridation; Internal nitridation; Microstructure; Diffusion; Kinetics; Layer growth

1. Introduction

The Nb–Ti–N system has been the subject of several investigations mainly regarding the interesting superconducting properties of the δ -(Nb,Ti)N phase. Complete solubility between δ -NbN and δ -TiN is reported and the superconducting critical temperature (T_c) presents a broad maximum between 30 and 60 mol.% TiN [1–3]. The maximum measured value is about 18 K [1] to be compared with the T_c of Ti–Nb alloys (9.5 K), the most widely used superconducting material. The higher T_c and a low radio-frequency surface resistance [4] make δ -(Nb,Ti)N an attractive material for potential applications in superconducting devices and in particular in superconducting resonators. A compact δ -nitride thick film can be easily obtained at the surface of Ti–Nb alloys by nitriding under appropriate nitrogen pressures at high temperature. De-

vices with complex shape can be realized by appropriate shaping or machining of the original alloy and, if necessary, by electron-beam welding of different components. Superconducting radio-frequency cavities with promising performances have been recently produced using this procedure [4]. The presence of a residual alloy core gives reasonable mechanical properties to the final nitrided cavity.

Although the binary systems, Nb–Ti [5], Ti–N [6,7] and Nb–N [8–10], have been extensively studied, little is known about the ternary Nb–Ti–N [11]. When Nb–Ti alloys are exposed to a nitrogen atmosphere, formation of a surface nitride layer as well as of internal nitride precipitates occurs, as observed for other binary and more complex alloys [12,13]. Internal nitridation is related to the large permeability of nitrogen in Nb–Ti alloys and to the higher thermodynamic stability of TiN in comparison to niobium nitrides. The nitriding behaviour of Ti–Nb alloys in nitrogen was studied by Felten [14] and more recently

*Corresponding author. E-mail: buscaglia@icfam.ge.cnr.it

by Buscaglia et al. [4,15] and by Mayr et al. [16]. After nitridation formation of a surface nitride layer and of Ti-rich needle-like precipitates at the interior of the alloy were observed. Homogeneous, fully nitrated plane-sheet samples were used for measurements of lattice parameters, microhardness and superconducting T_c of δ -(Nb,Ti)N [16]. The properties showed a strong dependency upon the Nb/Ti ratio as well as on the N content.

The present work was carried out to investigate microstructure evolution, phase composition and nitridation kinetics of Ti–Nb alloys of different composition exposed to a nitrogen atmosphere at high temperatures with a twofold purpose: to get insight into the mechanism of high-temperature nitridation of transition metal alloys and to obtain useful information for the fabrication technology of δ -(Nb,Ti)N superconducting devices.

2. Experimental

Four different Nb–Ti alloys (10, 47, 63 and 90 at.% Ti) were selected as starting materials. The alloy with 63 at.% Ti is commercially available (Teledyne Wah Chang, Albany, USA, Ta 800 ppm, O 600 ppm, Hf<250 ppm, Zr<150 ppm, N, C, Si, W, Sn<60 ppm) and usually used for the production of superconducting cables. The other compositions were obtained by melting in a plasma furnace under helium (ITM-CNR, Lecco, Italy) and cold rolling. Square samples (1×1 cm) were cut from plane sheets \approx 0.1 cm thick and etched in a (1:1:2) mixture of HNO₃, HF and H₃PO₄ to remove several micrometres of alloy from the surface, possibly polluted by the machining. A few ‘wedge-type’ samples (tip angle \approx 20°) were cut from ingots obtained by arc melting of powder mixtures (Ti: Nisso, Japan, 99.7 wt.%; Nb: Goodfellow, UK, 99.85 wt.%) and homogenised at 1300°C for 6 h under 0.1 bar argon. As the thickness is variable in such specimens, near-tip regions of wedge-type samples will present high nitrogen saturation than far-tip regions after reaction. Microstructure and composition evolution as a function of nitrogen saturation can then be studied on a single sample rather than on a series of plane specimens with different thicknesses [17]. Plane sheet samples were nitrated at 1300, 1450 and 1600°C for times ranging from 0.5 to 16 h under 0.3 bar high-purity nitrogen (Carbogas, total impurities \approx 1 ppm). A high-vacuum furnace (Varian) equipped with tungsten heating elements and radiation shields was used. Before reaction, the samples were annealed for 30 min at 1200°C under high vacuum (\approx 10⁻⁵ Pa mbar); the temperature was then increased to the experimental set-up and nitrogen was introduced. Nitridation can be then considered to occur in a large-grained, well recrystallized material. The total amount of impurities present in the reaction atmosphere was estimated by mass-spectroscopy to be \approx 10 ppm. The cooling of the samples was quite slow; several minutes were required to reach

800°C. Wedge-type samples were reacted at 1300–1600°C in a cold-wall autoclave equipped with a tungsten heating tube under 3 and 30 bar high-purity nitrogen atmosphere. In this case the samples were cooled down to room temperature within a minute. Both plane-sheet and wedge-type specimens were embedded in cold-setting epoxy resin, cut and polished using 3 μ m diamond paste for 2–4 h. A final polishing stage with an aqueous silica colloidal suspension (Struers Mastermet) for 10–15 min was performed for optimal phase identification. Microstructure was observed by scanning electron microscopy (SEM, Philips 515) and polarized light microscopy (OM, Reichert). Phase identification was carried out on plane-sheet samples by X-ray diffraction in Bragg–Brentano geometry (Philips PW1710, CoK α , secondary monochromator). Diffraction patterns were taken, for some samples, as a function of depth by stepwise removal of layers on SiC emery paper. Niobium and titanium composition profiles in nitrated samples were measured by energy-dispersive spectroscopy (EDS, EDAX PV9900). The plane-sheet samples were also investigated for the overall nitridation kinetics (weight gain) and the nitride layer growth kinetics (layer thickness). Wedge-type samples were mainly investigated for the measurement of nitrogen, niobium and titanium atomic fraction in the different phases by wavelength-dispersive electron-probe microanalysis (EPMA, Cameca SX50). The EPMA setup for the system Nb–Ti–N is given in Ref. [16]. Nitridation under high pressure (30 bar) leads to the formation of thicker nitride layers which are more suitable for EPMA than layers formed at 3 and 0.3 bar.

3. Results

3.1. Microstructure and phase composition

The surface of the reacted samples was coloured by different shades of gold yellow depending on the original composition: from dark yellow (90 at.% Ti), to yellow (63 and 47 at.% Ti) and pale yellow (10 at.% Ti). The gold yellow colour is typical of the δ -(Ti,Nb)N nitride. XRD showed only the presence of phases isostructural with those of Nb–Ti, Nb–N and Ti–N binary systems; no individual ternary compounds were detected. Phases isostructural with γ -Nb₄N₃ or η -NbN were not observed. A layer of δ -(Nb,Ti)N (fcc structure) was present at the surface of all the reacted samples. The thickness of the surface nitride layer strongly depends, at constant temperature, on the Ti/Nb ratio in the original alloy and the nitrogen pressure as shown in Table 1. The thickness decreases as pressure decreases and has a minimum for the composition Ti₆₃Nb₃₇. The phase band sequence and the general microstructure of the reacted samples are in most cases independent of both temperature and reaction time for a given alloy composition. A similar microstructure

Table 1

Average thickness of the δ -(Ti,Nb)N surface layer measured on Nb–Ti alloys reacted at 1600°C for 8 h (sample thickness=0.1 cm)

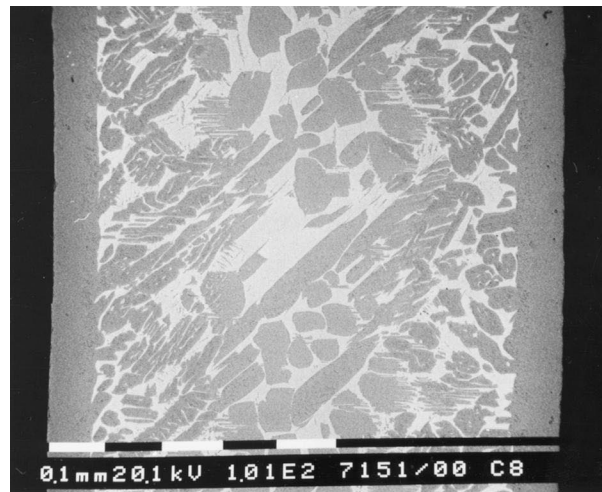
Alloy composition (at.%)	$p = 30$ bar [μm]	$p = 3$ bar [μm]	$p = 0.3$ bar [μm]
Ti ₉₀ Nb ₁₀	147	139	103
Ti ₆₃ Nb ₃₇	60	49	4–5
Ti ₄₇ Nb ₅₃	63	47	8–10
Ti ₁₀ Nb ₉₀	156	112	46
Nb	186	144	56 ^a

^a1670°C, 0.15 bar.

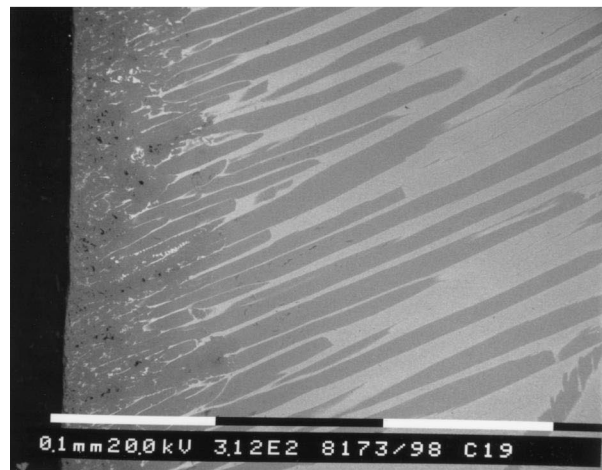
and the same phase composition were observed on plane and wedge-type samples for comparable nitrogen saturation levels. However, microstructure evolution is very different depending on the original composition.

3.1.1. Ti₉₀Nb₁₀

A cross section of a Ti₉₀Nb₁₀ plane sample reacted for 4 h at 1600°C is shown in Fig. 1a. The thick external scale corresponds to δ -(Ti,Nb)N; the large needles and islands (dark grey) present at the centre of the sample are composed of α -(Ti,Nb)(N) solid solution (hexagonal structure). The white phase corresponds to the residual alloy matrix β -(Ti,Nb). Microstructure evolution vs. time clearly indicates that internal nitridation mostly occurs by growth and enlargement of the existing precipitates rather than by formation of new inclusions. The α -phase precipitates close to the external layer are progressively converted to δ -(Ti,Nb)N as the reaction time increases. The difference in the grey level ($\approx 250 \mu\text{m}$ below the surface) indicates the α - δ transition in Fig. 1a. The microstructure observed at 1450°C is similar to that at 1600°C, whereas at 1300°C a clear distinction between the external layer and the internal nitridation zone no longer exists, as shown in Fig. 1b. The innermost part of the external layer and the precipitates of δ -(Ti,Nb)N undergo a transformation to ϵ -Ti₂N (tetragonal structure) because of the low cooling rate. The transformation can be suppressed by more rapid cooling as in the case of cold-wall autoclave. The phase ϵ -Ti₂N can be easily identified by polarized light microscopy because of its high optical anisotropy [17], as shown in Fig. 2. The N, Nb and Ti composition profiles measured on a Ti₉₀Nb₁₀ wedge-type sample annealed for 50 h at 1450°C are shown in Fig. 3. The profiles were obtained by a line scan performed on a far-tip region (thickness 2750 μm) and correspond to a microstructure similar to that reported in Fig. 1a. Examination of Fig. 3 reveals Nb enrichment in the β -(Ti,Nb) phase (up to 25–27 at.% when β phase is in contact with δ -(Ti,Nb)N, up to 20–22 at.% when β phase is in contact with α -(Ti,Nb)(N)). In turn, the α -(Ti,Nb)(N) and δ -(Ti,Nb)N phases are depleted in Nb in comparison to the original alloy composition. Composition profiles measured on a near-tip region (thickness 1100 μm) of the wedge-type sample show that the precipitates are completely converted in δ -(Ti,Nb)N and the niobium fraction in the



(a)



(b)

Fig. 1. Microstructure (SEM-BS images) of Ti₉₀Nb₁₀ nitrided under 0.3 bar nitrogen. (a) 4 h at 1600°C; (b) 2 h at 1300°C. External layer: δ -(Ti,Nb)N and ϵ -Ti₂N; needlelike precipitates: ϵ -Ti₂N and α -Ti(N); matrix: residual β -(Ti,Nb) alloy.

residual β -phase is ≈ 50 at.%. Niobium is isostructural with β -Ti (bcc structure) and concentrates in the β -(Nb,Ti) phase. Since the enrichment is higher near the surface than in the core, a metal concentration gradient sets up. On the contrary, even in near-tip regions of the wedge-type sample, the Nb fraction in the δ -(Ti,Nb)N phase is comparable to the values of Fig. 3 (≈ 3 at.%). These results were also confirmed by EDS analyses. Terminal nitrogen solubility in β -(Ti,Nb) is much lower than in α -(Ti,Nb) according to the data reported for pure metals: ≈ 2 at.% in Nb [18] and ≈ 25 at.% in α -Ti [7] at 1450°C.

3.1.2. Ti₆₃Nb₃₇ and Ti₄₇Nb₅₃

The microstructure of alloys containing 63 and 47 at.% Ti is characterized by the presence of elongated, needle-like, precipitates of δ -(Ti,Nb)N, as shown in Fig. 4 and Fig. 5. Where the growth of the precipitates is not disturbed by the grain boundaries of the alloy, the develop-

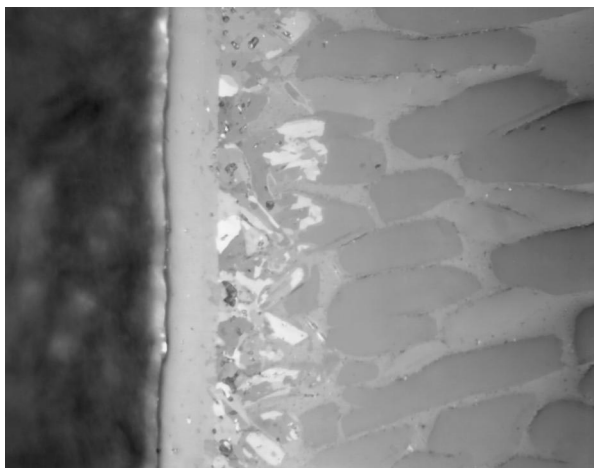


Fig. 2. Microstructure (OM, polarized light) of $Ti_{90}Nb_{10}$ nitrided at $1450^{\circ}C$ for 8 h. External layer (light grey): δ -(Ti,Nb)N; underlying layer (light and dark crystallites): ϵ - Ti_2N ; needlelike precipitates (dark grey): α -Ti(N); matrix (light grey): residual β -(Ti,Nb) alloy.

ment of ordered patterns resulting from the growth of long, parallel, δ -(Ti,Nb) needles inside the alloy matrix can be observed. The precipitates develop strong orientation relationships with the bcc β -(Ti,Nb) alloy matrix, as evident from microstructure. Different grain orientations in the alloy are 'imaged' by different orientations of the needles. Moving from the tip of the needles towards the sample surface the spacing between the needles is approximately constant at the beginning and then gradually decreases with formation of shorter needles between the longer ones. Near the surface the needles become much thinner and closely spaced. Internal nitridation thus mainly occurs by the progressive lengthening and thickening of the existing precipitates. When the needles coming from opposite sides meet at the centre of the sample, they stop to grow. However, internal nitride formation still continues by coarsening of the needles. In the case of $Ti_{63}Nb_{37}$, the

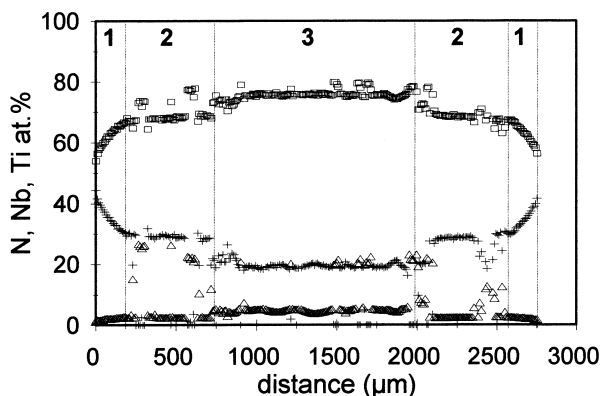


Fig. 3. Nitrogen, niobium and titanium profiles (EPMA) in a Nb-Ti wedge-type diffusion couple ($Ti_{90}Nb_{10}$, $T=1450^{\circ}C$, $p=30$ bar N_2 , sample thickness: $2750 \mu m$). (+) N; (Δ) Nb; (\square) Ti. Region (1): δ -(Ti,Nb)N; region (2): δ -(Ti,Nb)N + β -(Ti,Nb); region (3): α -(Ti,Nb)(N) + β -(Ti,Nb).

typical composition of the needles observed on a wedge-type sample nitrided for 50 h at $1450^{\circ}C$ (sample thickness $3000 \mu m$) change from 31.7 at.% N, 3.7 at.% Nb and 64.6 at.% Ti at the centre to 47.8 at.% N, 3.1 at.% Nb and 49.1 at.% Ti near the surface. As a consequence of preferential TiN segregation, the residual β alloy is progressively depleted in Ti and enriched in Nb moving from the centre (50.9 at.% Nb, 49.1 at.% Ti) to the near-surface region (97.0 at.% Nb, 3.0 at.% Ti). In the case of $Ti_{47}Nb_{53}$, the behaviour is very similar: the composition of the precipitates (sample thickness $3000 \mu m$) changes from 38.6 at.% N, 3.3 at.% Nb and 58.1 at.% Ti (centre) to 47.7 at.% N, 4.5 at.% Nb and 47.8 at.% Ti (near surface) and the alloy is gradually enriched in Nb (75.6 at.% at the centre, 95.8 at.% near the surface). The Nb profile as measured by energy dispersive microprobe analysis along single δ -(Ti,Nb)N needles and the average composition of the surrounding alloy on $Ti_{63}Nb_{37}$ plane samples are reported in Fig. 6. The Nb content in the needles is almost constant (≈ 5 at.%) in agreement with the WDS results. The external δ -(Ti,Nb)N nitride layer is very thin and can be only observed at high magnification on samples reacted at $1600^{\circ}C$ for the longer times (Fig. 4c and Fig. 5c). The composition obtained by EDS analysis of the external layer of samples reacted for 8 h at $1600^{\circ}C$ is 45–55 at.% Nb for $Ti_{63}Nb_{37}$ and 49 at.% Nb for $Ti_{47}Nb_{53}$ (N excluded). A rough estimate of the average composition of the surface layer from the cell parameter of δ -(Ti,Nb)N as determined by XRD gives ≈ 55 mol.% NbN for $Ti_{63}Nb_{37}$ and ≈ 50 mol.% NbN for $Ti_{47}Nb_{53}$. Below the surface layer a thin and irregular layer of β - Nb_2N containing small δ -(Ti,Nb)N needles was also detected (Fig. 4c and Fig. 5c). Composition profiles collected on the near-tip region of the wedge-type sample (thickness $750 \mu m$) show that the composition of the δ -(Ti,Nb)N needles is almost constant: 46 at.% N, 51 at.% Ti and 3 at.% Nb. The residual metallic phase is composed of 98 at.% Nb and 2 at.% Ti.

3.1.3. $Ti_{10}Nb_{90}$

The alloy containing 90 at.% Nb presents, as well as observed for the other compositions, both internal and external nitridation (Fig. 7a). The external scale is formed by an outer δ -(Nb,Ti)N layer and an inner β -(Nb,Ti) $_2$ N layer. The precipitate particles inside the alloy are composed of β -(Nb,Ti) $_2$ N. Both intra- and intergranular precipitation can be observed. The precipitates morphology in the intragranular precipitation zone at 1450 and $1600^{\circ}C$ corresponds to both small needles and approximately spherical fine particles (Fig. 7b). Sometimes thin bands parallel to the specimen surface originated by interconnected particles are observed. As a difference from Ti-richer alloys, internal nitridation mainly occurs by formation of new β -(Nb,Ti) $_2$ N particles in the internal precipitation zone and along grain boundaries. Formation of ordered lamellar structures, similar to those encountered in discontinuous precipitation and in eutectic decomposition

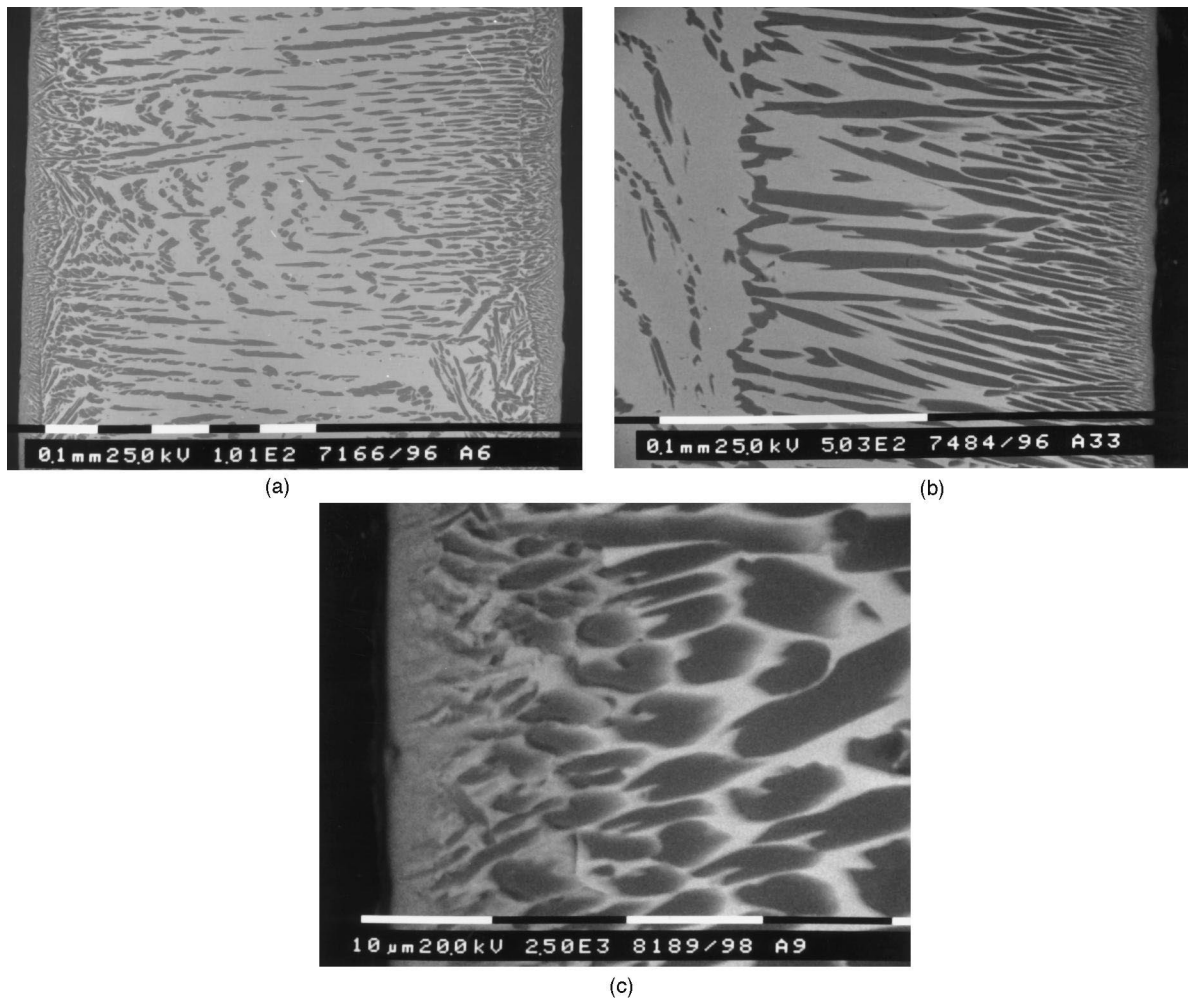


Fig. 4. Microstructure (SEM-BS images) of $Ti_{63}Nb_{37}$ nitrided under 0.3 bar nitrogen. (a) 2 h at 1600°C; (b) 0.5 h at 1600°C. Needlelike precipitates (dark grey): δ -(Ti,Nb)N; matrix (white); residual β -(Ti,Nb) alloy. (c) 8 h at 1600°C. From left to right: external layer of δ -(Ti,Nb)N, intermediate layer of β -(Nb,Ti) $_2$ N with small δ -(Ti,Nb)N needles and inner zone with δ -(Ti,Nb)N needles in a Nb-rich β -(Ti,Nb) phase.

were instead observed at 1300°C (Fig. 7c) and, locally, at 1450°C. The N, Nb and Ti composition profiles measured on a $Ti_{10}Nb_{90}$ wedge-type sample annealed 50 h at 1450°C are shown in Fig. 8 (sample thickness: 600 μ m). A substantial amount of Ti is present in both nitride layers, but the composition oscillates from 3 to 10 at.% Ti and this could be related to the progressive incorporation of precipitates during growth. The scattered points in the central portion of the profiles correspond to the presence of the precipitates inside the residual β alloy. EPMA measurements in this region were difficult to perform since the nitride precipitates are of a size (≤ 5 μ m) comparable or lower than the lateral resolution of the technique. EDS analyses performed on the β -(Nb,Ti) $_2$ N largest particles present in a sample annealed 16 h at 1450°C give up to 15 at.% Ti (N excluded). As difference from the Ti-richer alloys, the composition of the different phases measured on the wedge-type sample does not show a significant dependence on the thickness.

3.2. Kinetics

The weight gain kinetics of the different alloys is shown in Fig. 9a–c, plotted according to the parabolic rate equation

$$W = \sqrt{2k_p t} \quad (1)$$

where W is the weight gain per unit area ($g\ cm^{-2}$) measured after a time t and k_p is the parabolic rate constant. The measured weight gain corresponds to the sum of three different contributions: external scaling, internal nitridation and nitrogen dissolution in the alloy. At 1300°C, the data are well described by straight lines crossing the origin, meaning that the above equation holds and, as a consequence, the nitridation is controlled by solid-state diffusion. At higher temperature, 1450 and 1600°C, the parabolic behaviour is observed only for short reaction times (up to ≈ 2 –4 h at 1450°C and up to ≈ 1 –2 h

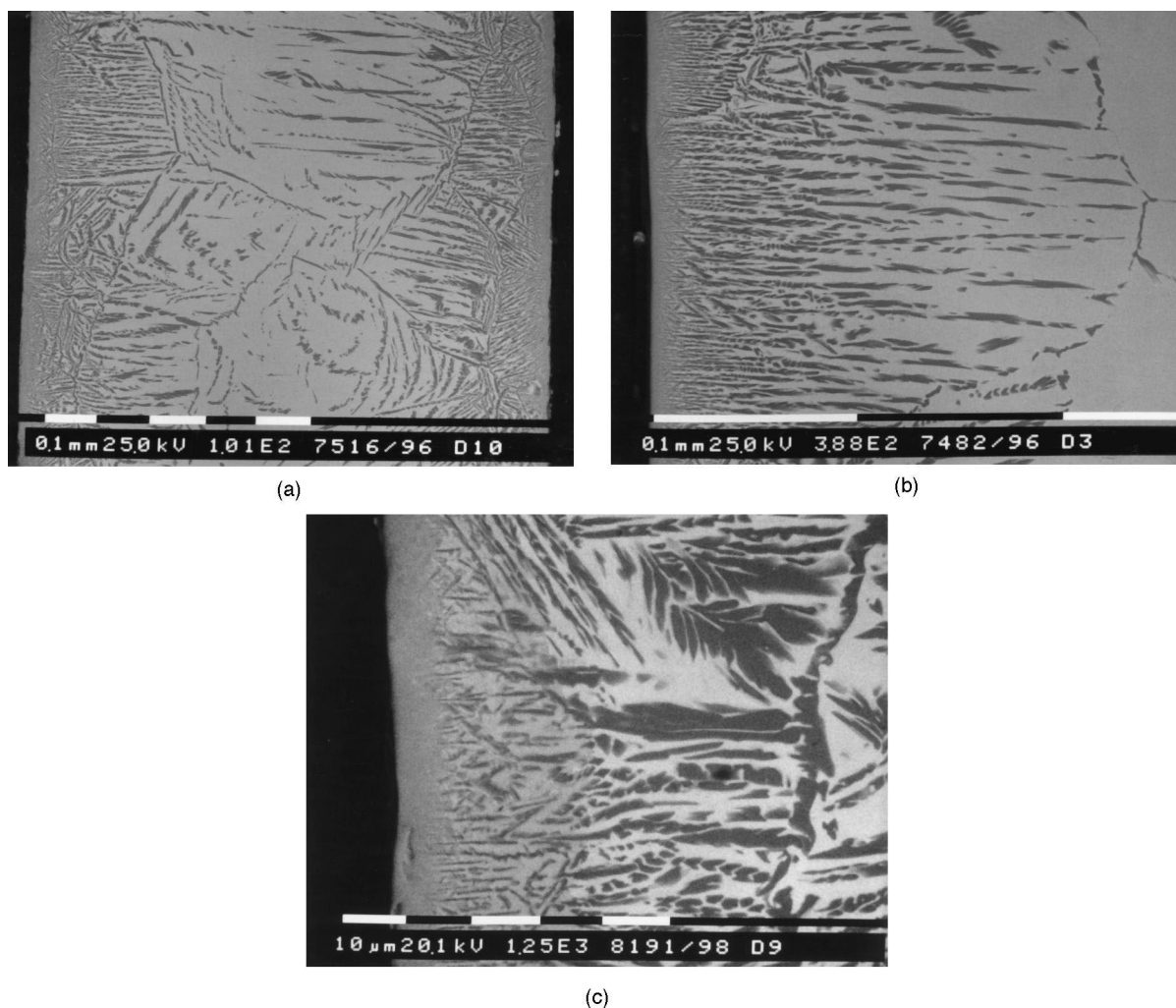


Fig. 5. Microstructure (SEM-BS images) of $Ti_{47}Nb_{33}$ nitrided under 0.3 bar nitrogen. (a) 2 h at 1600°C; (b) 0.5 h at 1600°C. Needlelike precipitates (dark grey): δ -(Ti,Nb)N; matrix (white): residual β -(Ti,Nb) alloy. (c) 8 h at 1600°C. From left to right: external layer of δ -(Ti,Nb)N, intermediate layer of β -(Nb,Ti)₂N with small δ -(Ti,Nb)N needles and inner zone with δ -(Ti,Nb)N needles in a Nb-rich β -(Ti,Nb) phase.

at 1600°C). At longer times the rates decline to lower values, corresponding to the approach to saturation of the alloy core with nitrogen and the slowing down of internal precipitation. This behaviour is typical of metals and alloys having non-negligible nitrogen solubility coupled with rapid nitrogen inward diffusion, as many of the transition metals. Alloy $Ti_{90}Nb_{10}$ shows a steep decrease of the nitridation rate after the initial parabolic stage, which is not observed for the other compositions. The values of k_p corresponding to the initial parabolic stage are reported in Table 2. The standard error is in any case <5%. The parabolic constant is strongly dependent on the original alloy composition and decreases as the niobium content increases. For the alloys $Ti_{90}Nb_{10}$ and $Ti_{10}Nb_{90}$ measurement of the thickness of the external nitride layers was possible and the layer growth kinetics is reported in Fig. 10 and Fig. 11. The effect of nitrogen saturation is well evident; a remarkable deviation from the initial parabolic

rate law is observed at 1450 and 1600°C for both compositions. In the case of $Ti_{10}Nb_{90}$ the layer growth rate increases in comparison with the initial kinetics whereas for $Ti_{90}Nb_{10}$ it decreases. The relative importance of the external nitridation process was estimated by comparing the total nitrogen uptake with the nitrogen contained in the external nitride layer(s). In order to simplify the calculation, the nitrogen concentration profile inside the layers was assumed to be linear and the concentration at the interfaces was obtained from EPMA measurements. For the alloys with intermediate composition, the thickness of the external layer(s) is in any case very thin and contributes no more than $\approx 10\%$ to the overall nitrogen uptake. The results for the other compositions are shown in Table 3: the amount of nitrogen contained in the external nitride layer(s) is generally less than 50%. Considering the reported nitrogen terminal solubility in Nb [18] and β -Ti [7], nitrogen dissolution inside the alloy cannot account for

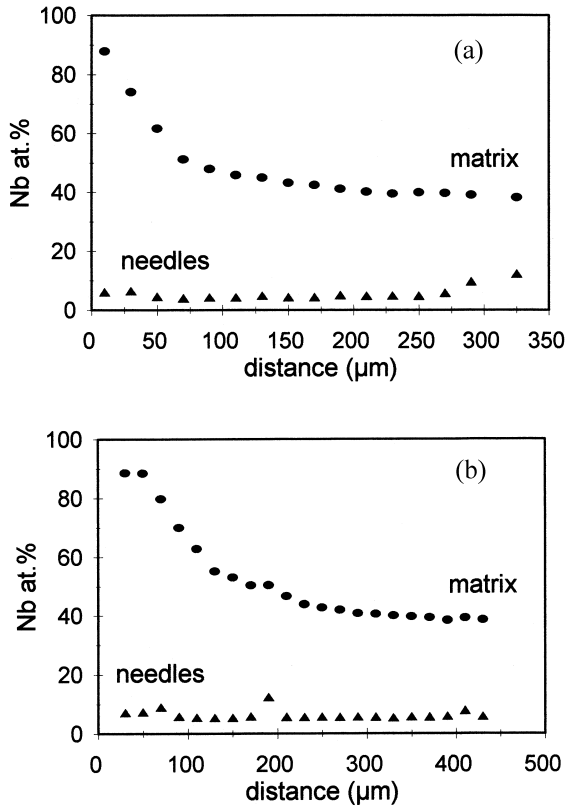


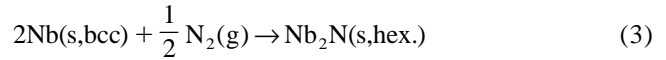
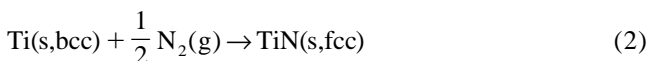
Fig. 6. Niobium profiles (EDS) in $Ti_{63}Nb_{37}$ nitrided under 0.3 bar nitrogen. (a) 2 h at 1450°C; (b) 1 h at 1600°C. (▲) δ -(Ti,Nb)N needles; (●) β -(Ti,Nb) matrix.

more than ≈ 10 –15 wt.% of the total nitrogen uptake. As a consequence, the internal nitride precipitation represents the main process occurring during nitridation of Ti–Nb alloys, except for $Ti_{90}Nb_{10}$ at 1600°C. The contribution of external scaling is approximately constant (at constant temperature) throughout the initial parabolic stage and the average value is reported in Table 3. About the non-parabolic stage, only the data corresponding to the longest reaction times are indicated. The contribution of external nitridation to the total nitrogen uptake increases in the non-parabolic stage and this is strictly related to the progressive saturation and the slowing down of internal nitridation.

4. Discussion

4.1. Phase formation in the Nb–Ti–N system

The nature and the sequence of the reaction products resulting from nitridation of Nb–Ti alloys can be qualitatively understood on the basis of the following reactions:



The equilibrium nitrogen partial pressures corresponding to the above reactions can be calculated using the available thermochemical data [19]. For example, at 1450°C, the equilibrium pressures are: $p_2 = 1.9 \times 10^{-11}$ atm; $p_3 = 5.9 \times 10^{-7}$ atm; $p_4 = 1.3 \times 10^{-3}$ atm.

Since $p_2 < p_3 < p_4$, TiN is thermodynamically more stable than the other nitrides present in the Nb–Ti–N system and, for a broad composition range extending from pure Ti towards Nb-rich alloys, a Ti-rich δ -(Nb,Ti)N phase will be the nitride in equilibrium with the metallic phase. However, as the difference in thermodynamic stability between TiN and Nb_2N is not so large, for alloys moderately rich in Nb (≥ 75 at.%), β - Nb_2N was observed to be the nitride in equilibrium with the alloy [16]. In such a case, where $p_4 > p_3$, a layer of Nb-rich δ -(Nb,Ti)N will grow on top of the β -(Nb,Ti) $_2$ N phase under the present experimental conditions. Since formation of γ - Nb_4N_3 and η -NbN during cooling down, as observed in the Nb–N system, no longer occurs, it can be concluded that the presence of TiN stabilizes the δ -(Ti,Nb) N_{1-x} phase in comparison to pure δ - NbN_{1-x} . It is well known that TiN has an almost constant composition close to the stoichiometric one for the nitrogen pressures utilized in this work (0.3 to 30 bar) in the range 1300–1600°C [17]. On the contrary, the composition of δ - NbN_{1-x} is strongly dependent on the applied pressure [8–10]. The growth rate of the external nitride layer is mainly determined by the difference between the mass fluxes that arrive at the inner interface and the mass fluxes which leave the inner interface. The surface composition, as well as the layer thickness of the δ -(Ti,Nb) N_{1-x} phase are therefore expected to be increasingly sensitive to the external nitrogen pressure moving from TiN to NbN_{1-x} . The thickness data reported in Table 1 show, in agreement, a strong dependence on nitrogen pressure even though the observed behaviour is not monotonic. A quantitative treatment of the diffusion fluxes is therefore required to explain the dependence of the δ -(Ti, Nb)N layer thickness on alloy composition.

Interstitial atoms like oxygen and nitrogen stabilize the α -Ti phase above the value of 883°C reported for the α – β phase transformation in high-purity titanium [7]. Therefore, when a titanium-rich alloy is exposed either to a nitrogen- or oxygen-containing atmosphere, formation of the α -Ti phase occurs by inward nitrogen or oxygen diffusion through the β phase. As we are dealing with reaction diffusion in a ternary system, development of non-planar interfaces between the different phases is possible. In particular, for $Ti_{90}Nb_{10}$, the α -(Ti,Nb)(N)

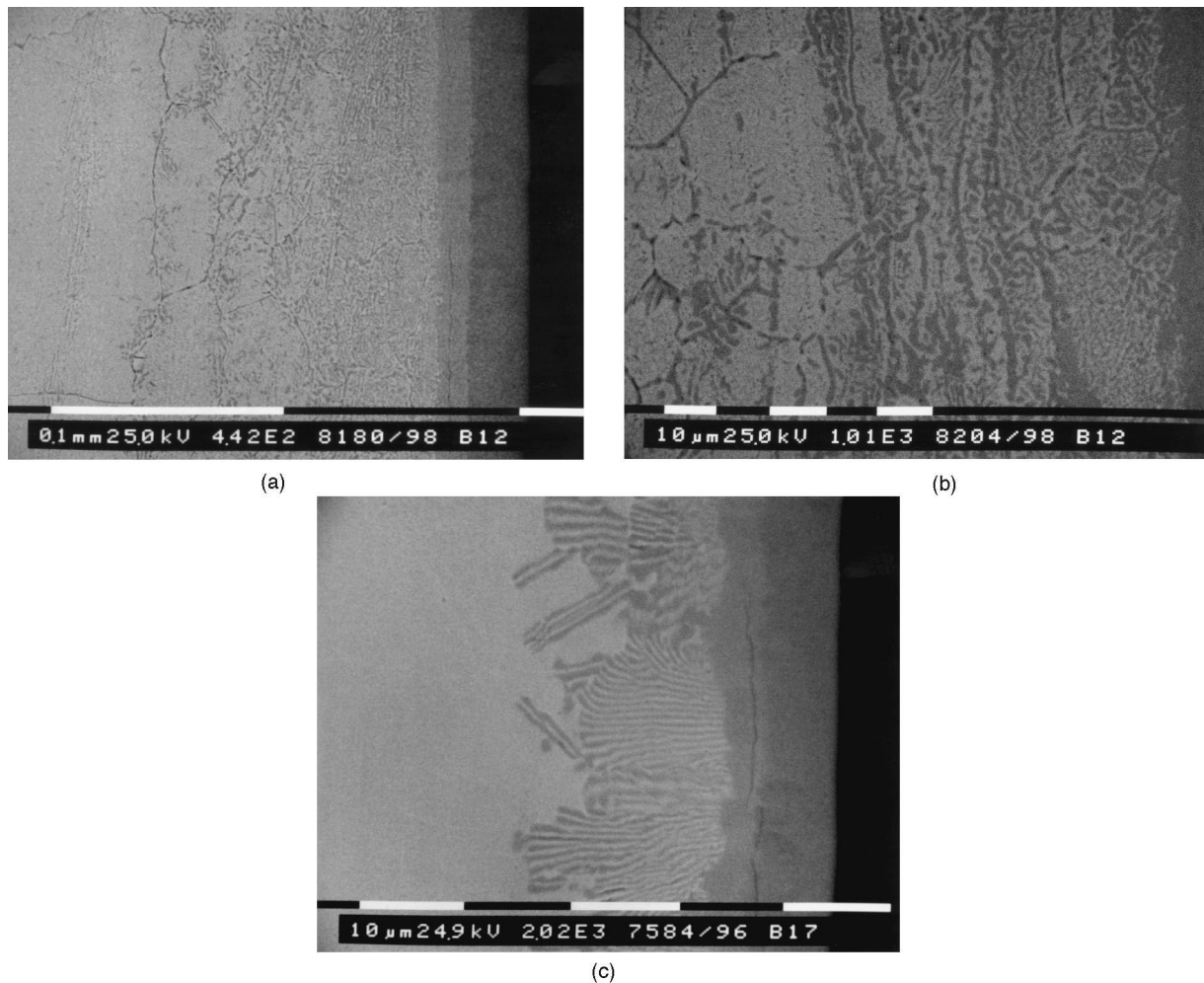


Fig. 7. Microstructure (SEM-BS images) of $Ti_{10}Nb_{90}$ annealed under 0.3 bar nitrogen. (a) Cross section of a sample nitrided 16 h at 1450°C; external layer: δ -(Nb,Ti)N; underlying layer: β -(Nb,Ti) $_2$ N; precipitates in the internal nitridation zone: β -(Nb,Ti) $_2$ N. (b) Magnification of the internal nitridation zone. (c) Cross section of a sample nitrided 12 h at 1300°C showing pearlite-like precipitation.

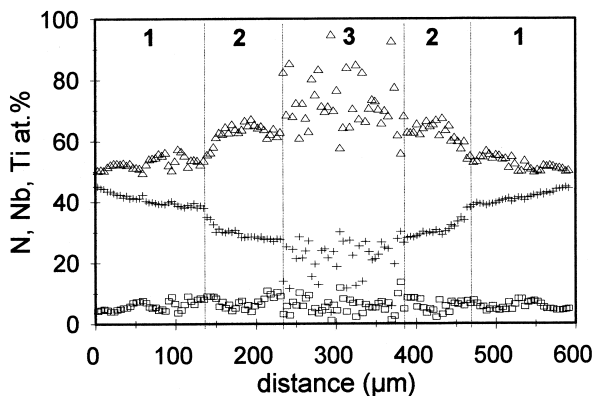


Fig. 8. Nitrogen, niobium and titanium profiles (EPMA) in a Nb-Ti-N wedge-type diffusion couple ($Ti_{10}Nb_{90}$, $T=1450^{\circ}C$, $p=30$ bar N_2 , sample thickness: 600 μm). (+) N; (Δ) Nb; (\square) Ti. Region (1): δ -(Nb,Ti)N; region (2): β -(Nb,Ti) $_2$ N; region (3): β -(Nb,Ti) matrix + β -(Nb,Ti) $_2$ N precipitates.

phase does not generate a continuous layer as observed for the nitridation of pure titanium, but grows in the form of large needles inside the β -(Ti,Nb) phase. Similar microstructures were reported in very different situations: HIP- and laser-nitriding of commercial Ti alloys like Ti-3.4Al-8.1V-5.9Cr-4.3Mo and Ti-6Al-4V [20,21], nitridation of Ti-Zr alloys [22], nitridation of Ti-V alloys [23], oxidation and oxy-nitridation of Ti-Ta alloys (5, 40 and 60 wt.% Ta) [24,25]. The resulting microstructure corresponds, in any case, to the formation of coarse α -Ti needles which develop strong orientation relationships with the β -Ti phase. The driving force which promotes microstructural evolution during phase transformation is the variation of the Gibbs' free energy between the metastable β phase and the α + β assembly. The magnitude of the driving force is roughly proportional to the level of supersaturation of the α -stabilizer (nitrogen or oxygen) in the β phase. As the same α / β two-phase microstructure is observed in rather different environments, probably one or

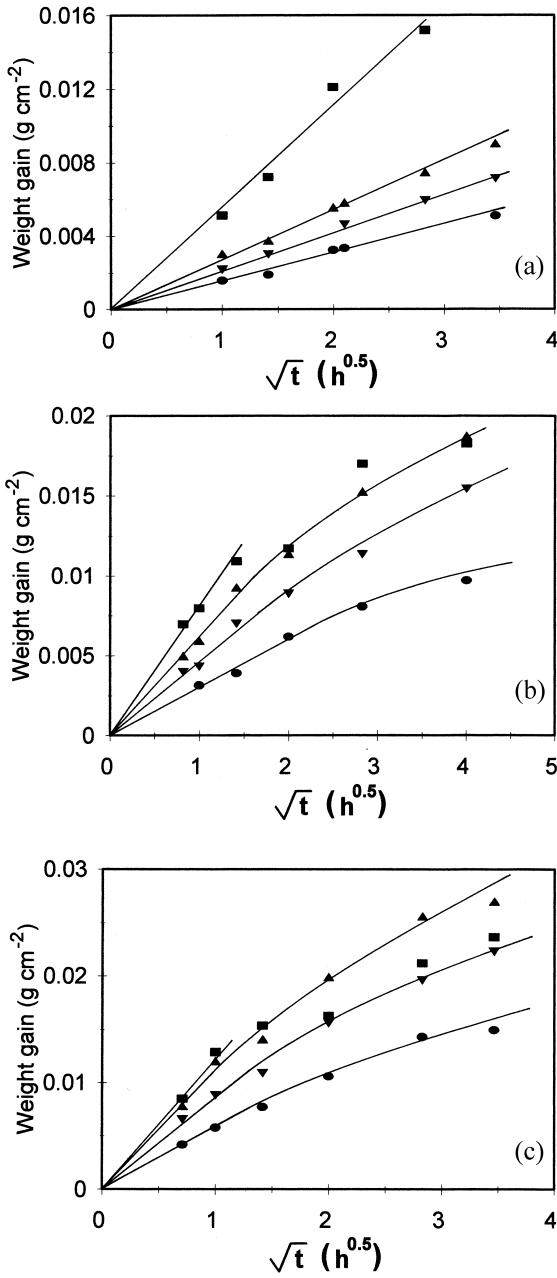


Fig. 9. Weight gain kinetics under 0.3 bar nitrogen. (■) Ti₉₀Nb₁₀, (▲) Ti₆₃Nb₃₇, (▼) Ti₄₇Nb₅₃, (●) Ti₁₀Nb₉₀. (a) 1300°C; (b) 1450°C; (c) 1600°C.

Table 2
 Values of the parabolic rate constant (g² cm⁻⁴ s⁻¹) corresponding to the initial nitridation stage (p=0.3 bar) of Nb–Ti alloys

T (°C)	Ti ₉₀ Nb ₁₀	Ti ₆₃ Nb ₃₇	Ti ₄₇ Nb ₅₃	Ti ₁₀ Nb ₉₀
1300	4.2 × 10 ⁻⁹	1.0 × 10 ⁻⁹	6.1 × 10 ⁻¹⁰	3.2 × 10 ⁻¹⁰
1450	8.7 × 10 ⁻⁹	5.0 × 10 ⁻⁹	2.9 × 10 ⁻⁹	1.2 × 10 ⁻⁹
1600	2.2 × 10 ⁻⁸	1.9 × 10 ⁻⁸	1.1 × 10 ⁻⁸	4.4 × 10 ⁻⁹

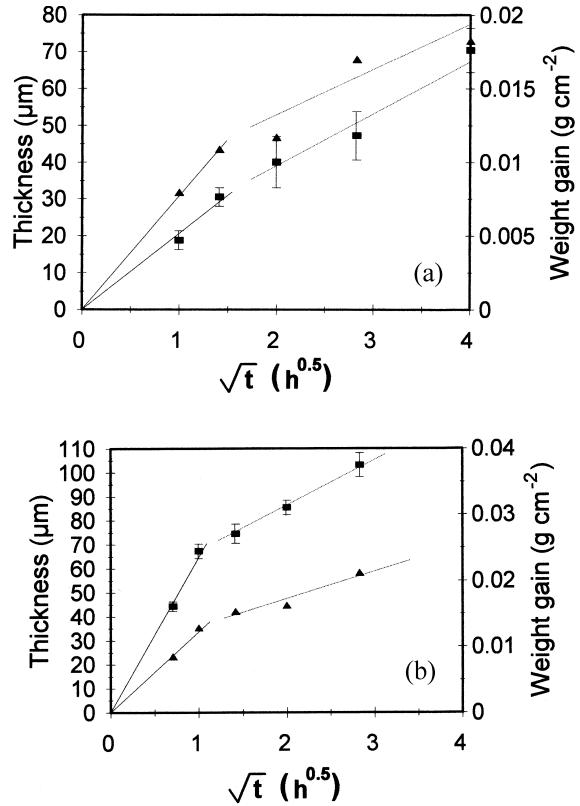


Fig. 10. Layer thickness (■: δ-(Ti,Nb)N) and weight gain (▲) vs. time of Ti₉₀Nb₁₀ nitrided under 0.3 bar nitrogen. (a) 1450°C; (b) 1600°C.

more common factors control the nucleation and growth of the precipitates.

4.2. On the nucleation of the internal nitride precipitates

The considerable size of the precipitates observed in the three Ti-rich alloys indicates that both homogeneous nucleation and nucleation on dislocation lines is difficult; heterogeneous nucleation at grain boundaries and on impurity sites as well as enlargement of the existing precipitates are the most favoured processes. A quantitative treatment of the nucleation problem is proposed in this section to support the microstructural observations.

Nucleation and growth of a solid inclusion in a solid matrix involves an elastic strain energy, ΔG_{strain} , related to the change of molar volume. The elastic strain energy reduces the effective driving force of the reaction, ΔG_{chem} . The term ΔG_{chem} corresponds to the Gibbs' free energy change per unit volume. The total free energy change for nucleation is, for a nucleus of generic shape, volume V and surface area A ,

$$\Delta G = (\Delta G_{\text{chem}} + \Delta G_{\text{strain}})V + \sigma A \quad (5)$$

where σ is the interfacial energy of the matrix/precipitate interface. Obviously, random homogeneous nucleation will only occur if $(\Delta G_{\text{chem}} + \Delta G_{\text{strain}}) < 0$. For a spherical

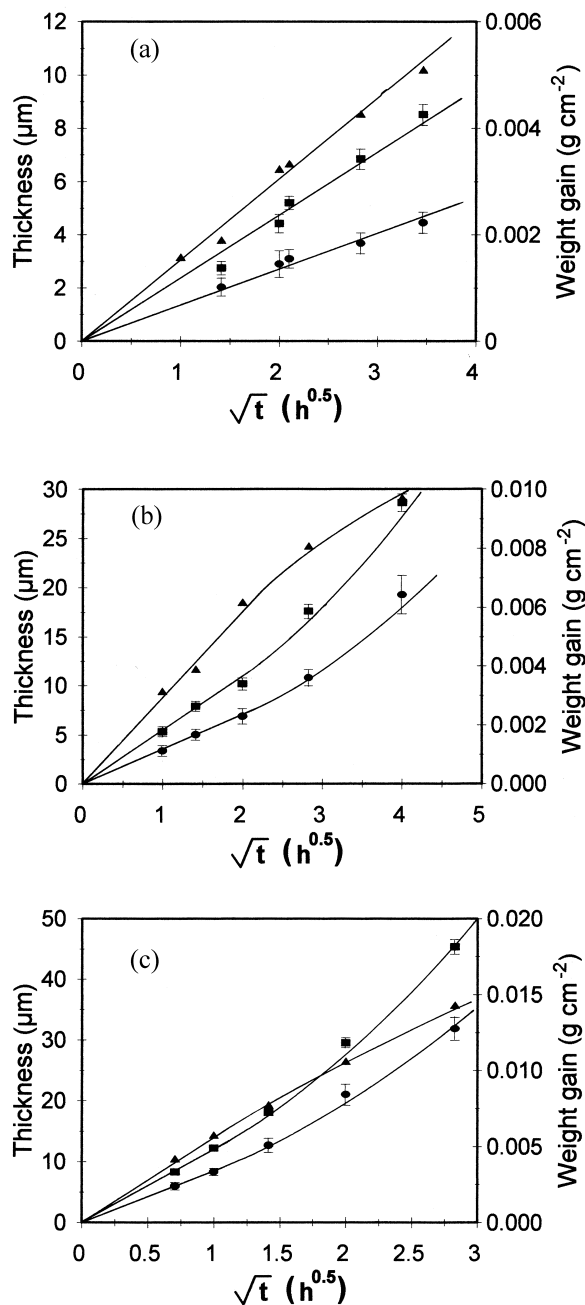


Fig. 11. Layer thickness (■: δ -(Nb,Ti)N; ●: β -(Nb,Ti)₂N) and weight gain (▲) vs. time of Ti₁₀Nb₉₀ nitrided under 0.3 bar nitrogen. (a) 1300°C; (b) 1450°C; (c) 1600°C.

Table 3
Contribution (wt.%) of the external nitride layer(s) to the overall nitrogen uptake ($p=0.3$ bar)

T (°C)	Ti ₉₀ Nb ₁₀		Ti ₁₀ Nb ₉₀	
	Parabolic stage	Non-parabolic stage	Parabolic stage	Non-parabolic stage
1300	Not observable ^a	–	18	–
1450	26	43	21	35
1600	58	54	24	38

Parabolic stage: mean values over different reaction times. Non-parabolic stage: values corresponding to the longest reaction time (16 h at 1450°C and 8 h at 1600°C).

^aIn this condition there was not a clear distinction between the external nitride layer and the internal precipitation zone.

precipitate particle, the classical nucleation theory gives for the Gibbs' free energy barrier ΔG^* corresponding to the formation of a critical nucleus and the radius R^* of the critical nucleus (see, for example, Ref. [26])

$$\Delta G^* = \frac{16}{3} \pi \frac{\sigma^3}{(\Delta G_{\text{chem}} + \Delta G_{\text{strain}})^2} \quad (6)$$

$$R^* = \frac{2\sigma}{-(\Delta G_{\text{chem}} + \Delta G_{\text{strain}})} \quad (7)$$

If the elastic strain energy becomes comparable with the absolute value of the Gibbs' free energy of reaction, both the free energy barrier and the radius of the critical nucleus will rise and the nucleation rate will strongly decrease. When ΔG^* is large enough, homogeneous nucleation will be hindered and, therefore, heterogeneous nucleation as well as the growth of the supercritical particles will be the most favoured processes.

In principle, provided that the elastic constants of the precipitate and the matrix are known, it is possible to calculate the elastic strain energy related to nucleation. The detailed calculation of the strain energy is presented in Appendix A and the results, corresponding to different interface types (coherent, incoherent) and different shapes of the inclusion (sphere, needle) are shown in Table 5. Because of the large uncertainty on the elastic constants available in the literature, the reported values represent only a rough estimate of the elastic strain energy. The precipitation of four different phases in the β -(Ti,Nb) matrix was considered: α -Ti, non-stoichiometric δ -TiN corresponding to the composition TiN_{0.5}, stoichiometric δ -TiN and β -Nb₂N. The computed ΔG_{strain} values should be considered as an upper limit. For precipitation of α -Ti(N) and δ -TiN the volume misfit between precipitate and matrix is of the order of a few percent and could be accommodated largely elastically. On the contrary, in view of the large volume misfit corresponding to β -Nb₂N precipitation and the high temperatures, full elastic accommodation is unlikely and partial stress relaxation via plastic deformation of the matrix is expected. As a consequence, the effective values of ΔG_{strain} will be lower than that predicted by the elastic theory and reported in Table 5. An underestimate of ΔG_{strain} is in any case zero.

The calculation of the term ΔG_{chem} requires the knowledge of the thermodynamic functions of the Nb–Ti–N system. The only existing ternary phase diagram [11] is not reliable to estimate the Gibbs' free energy function because it does not report the α -(Ti,Nb)(N) and the β -(Nb,Ti)₂N phases. The term ΔG_{chem} was therefore calculated for two limiting situations corresponding to the binary systems: precipitation of α -Ti(N) in supersaturated β -Ti(N) and precipitation of β -Nb₂N in supersaturated Nb(N). The calculation details are presented in Appendix B. The conditions adopted should correspond to those existing in the alloy below a surface nitride layer. Even though the effect of the third element is neglected, the calculated values should give the correct order of magnitude of the chemical driving force at least for precipitation in Ti-rich and in Nb-rich alloys. The nitrogen supersaturation level in the matrix plays a critical role, as the Gibbs' free energy change ΔG_{chem} is roughly proportional to this parameter. A supersaturation of 10% is usually assumed in the treatment of nucleation problems. However, nucleation of β -(Nb,Ti)₂N at the internal precipitation front in Ti₁₀Nb₉₀ might involve much higher supersaturation values. A strong increase of nitrogen solubility has been reported to occur during internal nitridation of Fe–Cr, Fe–Ti and Fe–Al alloys [27–29]. This 'excess' nitrogen has been ascribed to a dilation of the matrix related to the elastic accommodation of misfit between small coherent nitride particles and the matrix. In addition, 'excess' nitrogen can be associated with dislocations generated during precipitation of incoherent particles. As a consequence, two further supersaturation levels were considered: 20 and 50%. The chemical Gibbs' free energy available for the precipitation reaction is reported in Table 6 for the nucleation of α -Ti(N) in β -Ti(N) and in Table 7 for the nucleation of β -Nb₂N in Nb(N). Inspection of the calculated strain energy values (Table 5) and of the Gibbs chemical free energy (Tables 6 and 7) leads to different considerations.

The order of magnitude of the elastic strain energy does not depend remarkably on the type of matrix/inclusion interface (coherent or incoherent) as well as on the particle morphology (spheres or needles).

The chemical Gibbs free energy change is in any case small; at 1450°C, considering 10% supersaturation, is -242 J mol^{-1} (-22.2 MJ m^{-3}) for the β -Ti \rightarrow α -Ti transformation and -830 J mol^{-1} (-34.5 MJ m^{-3}) for the formation of β -Nb₂N from Nb(N). For sake of comparison, the free energy change of the γ \rightarrow α phase transition in iron at 1392°C is $-39\,600 \text{ J mol}^{-1}$ [19]. Formation of β -Nb₂N involves values of ΔG_{chem} (per unit volume) which are 1.5–2 times more negative than those for formation of α -Ti(N).

For the β -Ti(N) \rightarrow α -Ti(N) transformation the chemical Gibbs free energy change (-20 to -40 MJ m^{-3}) is of the same order of magnitude (absolute value) of the elastic strain energy ($\approx 20 \text{ MJ m}^{-3}$). Even in the limiting situation

$\Delta G_{\text{strain}}=0$, assuming σ in the range 0.1 (coherent interface) to 1 (incoherent interface) J m^{-2} , Eq. (6) gives a free energy barrier much greater than 74 kT, the quoted critical value which corresponds to the lower limit of 1 nucleus per cm^3 per s to the observable nucleation rate [26]. To lower ΔG^* to 74 kT, supersaturation should be greater than 50% when $\sigma=0.1 \text{ J m}^{-2}$. In these conditions homogeneous random nucleation will be anyway very difficult or even impossible. As a consequence formation of the α -phase will only occur at a limited number of sites through a heterogeneous nucleation mechanism.

Homogeneous nucleation of β -Nb₂N from Nb(N) is apparently inhibited, as the elastic strain energy (200 – 400 MJ m^{-3}) is much larger than the absolute value of the chemical Gibbs free energy change (-34.5 MJ m^{-3} at 1450°C for 10% supersaturation). To lower the energy barrier to the critical value of 74 kT ($T=1450^\circ\text{C}$) for viable nucleation the term $(\Delta G_{\text{chem}} + \Delta G_{\text{strain}})$ in Eq. (6) should be -97.5 MJ m^{-3} when $\sigma=0.1 \text{ J m}^{-2}$ or -3084 MJ m^{-3} when $\sigma=1 \text{ J m}^{-2}$. In the limiting situation $\Delta G_{\text{strain}}=0$, thus homogeneous nucleation of β -Nb₂N becomes possible at a supersaturation of $\approx 30\%$ for a coherent matrix/precipitate interface. This implies that a considerable fraction of the volume misfit has to be accommodated by plastic deformation. Plastic deformation of β (Ti,Nb) alloy should be quite easy in view of the high temperature and the large value of the elastic strain energy. As an alternative mechanism, precipitation of β -Nb₂N could occur through the formation of a hypothetical metastable phase. However, TEM investigations on nitriding of niobium in gaseous ammonia at 600–700°C [30] have shown that the small particles which appear at the beginning of precipitation are already composed of β -Nb₂N.

In addition to grain boundaries, dislocations can act as preferred sites for the formation of nuclei. If nucleation occurs on a dislocation line, in Eq. (5) there is an extra negative Gibbs energy contribution arising from the release of dislocation energy

$$\Delta G = (\Delta G_{\text{chem}} + \Delta G_{\text{strain}})V + \sigma A - \ell \Delta G_{\text{disl}} \quad (8)$$

where ΔG_{disl} and ℓ are the dislocation line energy and the length of the dislocation where energy has been released, respectively. The theory of nucleation on dislocation lines was first given by Cahn (see, for example, Ref. [26]), who considered the formation of a nucleus with circular cross section of radius r perpendicular to the dislocation line. For low driving forces there is a minimum in the free energy ΔG for $r=r_0$, followed by a maximum at a larger value of r . The difference in ΔG between the maximum and the minimum corresponds to the thermal barrier for nucleation on dislocations. For high driving forces, there are not turning points in ΔG and the energy of the nucleus decreases continuously as r increases (spontaneous nucleation). Thus there is a critical driving force at which the

maximum and the minimum merge together in an inflection point and the thermal barrier disappears. Following Cahn's approach [26], it is possible to calculate that, in the present case, a substantial reduction of the free energy barrier can be achieved by nucleation on dislocations, if the elastic strain energy is largely relaxed, so that the term ($\Delta G_{\text{chem}} + \Delta G_{\text{strain}}$) is close to ΔG_{chem} . Because of the larger driving force (see Tables 6 and 7), the lowering of the free energy barrier will be more pronounced for nucleation of $\beta\text{-Nb}_2\text{N}$. For example, taking $T=1450^\circ\text{C}$ and $\sigma=0.2\text{ J m}^{-2}$, the nucleation rate of $\beta\text{-Nb}_2\text{N}$ becomes appreciable ($1\text{ cm}^{-3}\text{ s}^{-1}$) at 20% supersaturation. The number of $\beta\text{-Nb}_2\text{N}$ precipitate particles per unit area at 1450 and 1600°C is of the order of 10^{11} m^{-2} , comparable with the dislocation density in well annealed pure metals ($10^{10}\text{--}10^{12}\text{ m}^{-2}$). On the contrary, precipitation of $\alpha\text{-Ti(N)}$ on dislocations become possible only at $\approx 50\%$ supersaturation ($\sigma=0.2\text{ J m}^{-2}$). The number of $\alpha\text{-Ti(N)}$ inclusions per unit area in $\text{Ti}_{90}\text{Nb}_{10}$ is, in agreement, orders of magnitude lower than the expected dislocation density. Impurities are likely to play an important role in the $\beta\rightarrow\alpha$ transformation by affecting the initial nucleation of the $\alpha\text{-Ti(N)}$ phase. After the initial nucleation stage, formation of new α phase will mainly occur by coarsening of the existing precipitates. The same conclusions probably hold also for precipitation of non-stoichiometric $\delta\text{-TiN}$, as the observed morphology is similar.

4.3. Microstructure evolution and diffusion

Precipitate morphologies are in most cases independent of temperature, in particular for the intermediate alloy compositions. As previously discussed, formation of nitride particles requires high supersaturation values. The morphology of the precipitates will be established during the first nitridation stage (parabolic stage) before appreciable saturation of the sample core occurs. In these conditions the inward nitrogen flux is large and high supersaturation levels can be achieved. In any case heterogeneous nucleation (impurities, grain boundaries, dislocations) is favoured in comparison to homogeneous nucleation. For alloys $\text{Ti}_{63}\text{Nb}_{37}$ and $\text{Ti}_{47}\text{Nb}_{53}$, the precipitates are much smaller and numerous immediately beneath the sample surface (see Fig. 4c and Fig. 5c) in comparison to the sample core (Fig. 4a and Fig. 5a). These particles were presumably formed at the very early stage of reaction, when the inward nitrogen flux is maximum. At longer times the nitrogen flux decreases and the enlargement of existing particles becomes the most favoured process. When the sample core approaches saturation, the nitrogen flux is further reduced and a decrease of the internal nitridation rate occurs. In the case of $\text{Ti}_{90}\text{Nb}_{10}$ alloy, the gradual conversion of the $\alpha\text{-(Ti,Nb)(N)}$ precipitates into $\delta\text{-(Ti,Nb)N}$ phase after the initial nitridation stage is observed. In fact, when the Nb concentration in the phase reaches a critical concentration ($\approx 20\text{ at.}\%$), the phase in

equilibrium with the alloy is no longer $\alpha\text{-(Ti,Nb)(N)}$, but becomes $\delta\text{-(Ti,Nb)N}$ (see Fig. 3). The transformation starts immediately beneath the external nitride layer and proceeds toward the interior of the sample, because the nitrogen activity must increase above the value corresponding to the $\alpha\text{-(Ti,Nb)(N)}/\beta\text{-(Ti,Nb)}/\delta\text{-(Ti,Nb)N}$ three phase equilibrium. For alloy $\text{Ti}_{10}\text{Nb}_{90}$, the precipitates are much smaller and do not develop strong orientation relationships with the matrix. In such a case, nucleation mainly occurs on grain boundaries and along dislocation lines and is less affected by the misfit strain energy. The much finer grain structure of $\text{Ti}_{10}\text{Nb}_{90}$ alloy in comparison to the other compositions can enhance intergranular precipitation because nitrogen diffusion along grain boundaries thereby become the predominant transport mechanism at the beginning of the nitridation process. In addition preferential segregation of one metal species can further affect grain boundary nucleation.

A general and important result is that the higher the Nb content the smaller the needles and the precipitates. This is in agreement with the observations reported in a previous work [16] regarding the nitridation of seven alloys of different composition; the size of the needles (both thickness and length) monotonously decreases as the Nb content increases while their number density increases. This indicates that the nucleation frequency changes over orders of magnitude depending on alloy composition.

Inward diffusion of nitrogen through the precipitation zone occurs predominantly through the $\beta\text{-(Ti,Nb)}$ phase because of the higher diffusivity. For instance, at 1450°C , nitrogen diffusivity ($\text{cm}^2\text{ s}^{-1}$) is $1\text{--}3\times 10^{-8}$ in niobium [31,32], $2\text{--}5\times 10^{-6}$ in $\beta\text{-Ti}$ [33–36], $1\text{--}5\times 10^{-8}$ in $\alpha\text{-Ti}$ [33–36], $1\text{--}3\times 10^{-9}$ in $\delta\text{-TiN}$ [33,36], $\approx 2\times 10^{-10}$ in $\beta\text{-Nb}_2\text{N}$ [31,32] and $\approx 7\times 10^{-10}$ in $\delta\text{-NbN}$ [31,32]. However, in samples $\text{Ti}_{63}\text{Nb}_{37}$ and $\text{Ti}_{47}\text{Nb}_{53}$, where formation of a large number of elongated $\delta\text{-(Ti,Nb)N}$ needles takes place, the alloy/nitride interfaces might represent a preferential diffusion path for nitrogen (short-circuit diffusion).

Niobium–titanium interdiffusion plays an important role in the internal precipitation process of the three Ti-rich alloys. Preferential titanium segregation in the nitride precipitates lead to titanium depletion in the β phase. The alloy will be progressively enriched in niobium moving from the centre to the surface, where the precipitates were formed at an early moment. This leads to the set up of a metal concentration gradient because of the relatively slow Nb–Ti interdiffusion in the β phase. At 1450°C the interdiffusion coefficient ($\text{cm}^2\text{ s}^{-1}$) is 1.0×10^{-8} for $\text{Ti}_{80}\text{Nb}_{20}$, 1.7×10^{-9} for $\text{Ti}_{60}\text{Nb}_{40}$, 1.9×10^{-10} for $\text{Ti}_{40}\text{Nb}_{60}$ and 2.5×10^{-11} for $\text{Ti}_{20}\text{Nb}_{80}$ [37]. Thus metal interdiffusion rapidly decreases as the Nb content increases. These values can be compared with nitrogen diffusivity ($\text{cm}^2\text{ s}^{-1}$) in niobium and $\beta\text{-Ti}$ at 1450°C : $1\text{--}3\times 10^{-8}$ [31,32] and $2\text{--}5\times 10^{-6}$ [33–36] $\text{cm}^2\text{ s}^{-1}$, respectively. Nitrogen diffusion is 2–3 orders of magnitude faster than metal interdiffusion. As a consequence,

because the growth rate of the precipitates is determined by the rate at which the precipitate-forming elements arrive at the precipitation site, long-range metal interdiffusion is likely to become rate-determining after the initial stage of reaction. In addition, formation of an external nitride layer where the Ti/Nb ratio is greater than that in the starting alloy can contribute to titanium depletion.

Precipitate morphologies corresponding to the formation of ordered lamellar structures ($\text{Ti}_{10}\text{Nb}_{90}$ nitrided at 1300°C, Fig. 7c) or colonies of needle-like particles ($\text{Ti}_{63}\text{Nb}_{37}$ and $\text{Ti}_{47}\text{Nb}_{53}$, Fig. 4 and Fig. 5) highlight the importance of lateral diffusion at the internal precipitation front. In such a case, the spacing of the lamellae or the needles reflects the distance over which Nb–Ti lateral interdiffusion occurs in the alloy. The application of the theory of discontinuous precipitation to nitridation of $\text{Ti}_{10}\text{Nb}_{90}$ [38] and coarse-grained $\text{Ti}_{63}\text{Nb}_{37}$ [15] at 1300°C, where the formation of ordered patterns is more evident, provide a satisfactory description of the growth mechanism of the precipitates. In both cases, the calculation gives a diffusivity value which is comparable with the order of magnitude of the metal interdiffusion coefficient in the β phase.

4.4. Nitridation kinetics

4.4.1. Overall kinetics

The reaction kinetics was parabolic at 1300°C and, for the shorter reaction times, also at 1450 and 1600°C. At longer times, the weight-gain kinetics declines to lower values (Fig. 9) as the sample core approaches saturation and internal precipitation slows down (see Table 3). The effect of temperature on the time at which deviation from the initial parabolic kinetics occurs is substantial. As nitrogen diffusivity in transition metals increases rapidly with temperature, core saturation is approached earlier in samples reacted at high temperature in spite of a larger nitrogen solubility. The effect of the finite thickness of the specimen on multiphase diffusion was first reported by Pawel [39] for the oxidation of zirconium alloys and, more recently, the problem of layer growth kinetics in finite gas–solid binary diffusion couples was analytically solved by Rafaja et al. [40]. At short time the concentration of nitrogen at the centre of the sample is virtually zero, the diffusion of nitrogen in the system can be treated as a multiphase diffusion problem in a semi-infinite geometry. The solution corresponds to the parabolic rate law defined by Eq. (1), where k_p is time-independent. At longer times, owing to the restricted geometry of the sample, the metal core approaches saturation, k_p in Eq. (1) is no longer time-independent, and a deviation from the initial parabolic kinetics is observed. The model is strictly correct for a binary or pseudo-binary system; in the present case deviations are expected owing to the presence of extensive internal precipitation, development of non-planar interfaces and metal interdiffusion. In particular, the model predicts

an increase of the growth rate of the nitride layers when the core of the sample approaches saturation in comparison to the thicknesses expected on the basis of the initial parabolic behaviour. This is actually observed for $\text{Ti}_{10}\text{Nb}_{90}$ (Fig. 11), but not for $\text{Ti}_{90}\text{Nb}_{10}$, where growth rate of the external TiN layer decreases after the initial parabolic stage (Fig. 10). In the latter case a sudden slowing down of the weight gain kinetics is also observed (Fig. 9b–c, Fig. 10). Different factors can contribute to the observed behaviour: (i) owing to the bulky nature of the α -Ti(N) needles, after the volume of the precipitates has reached a critical value, progressive impingement of the precipitates occurs. Therefore, the inward nitrogen flux through the β -(Ti,Nb) phase will be strongly reduced and in addition, diffusion must occur along a tortuous path. (ii) A large fraction of the inward nitrogen flux is consumed by the transformation of the α -Ti(N) precipitates in δ -(Ti,Nb)N. (iii) When the residual β -(Ti,Nb) phase is sufficiently enriched in Nb, the growth of the external δ -TiN layer may be controlled by the slower Nb–Ti interdiffusion rather than by nitrogen diffusion. It is not possible to decide what is the dominant factor on the basis of the currently available data.

4.4.2. Internal nitridation

In view of the large relative importance of internal precipitation (see Table 3), it can be inferred that the measured weight gain parabolic constants (Table 2) largely correspond to the internal nitridation reaction. The experimental results show that internal precipitation occurs by inward diffusion of nitrogen and involves long-range metal interdiffusion in the β -(Ti,Nb) phase (except for $\text{Ti}_{10}\text{Nb}_{90}$). The theory of internal precipitation during gas–alloy reactions was developed initially by Wagner for internal oxidation [41] and later extended by many authors to other kinds of reactions, like nitridation, carburization and sulphidation. An extensive review on the subject was published by Rapp [42]. The theory holds for precipitating compounds with high thermodynamic stability (low solubility product). An analytical expression of the depth of the precipitation zone as a function of the square root of time can be obtained assuming that the activity of both the penetrating and the precipitating elements drop to zero at the reaction front. Therefore precipitation occurs only at the reaction front and the amount of precipitate is constant throughout the whole internal precipitation zone. On the contrary, when the precipitating compound has only a ‘moderate’ stability (high solubility product), precipitation occurs continuously through the internal reaction zone, as theoretically discussed by Laflamme and Morral [43]. Deviations from Wagner’s classical treatment were reported for many systems, as recently reviewed by Douglass [44]. Christ et al. [45] have simulated the internal precipitation of a compound of moderate stability (solubility product: 5×10^{-4} , molar fraction basis) using a finite-differences technique to solve the diffusion equa-

tions. Their results are similar to the conclusions of Laflamme and Morral [43]. In particular the mole fraction of the precipitating element does not go to zero in the internal precipitation zone but decreases from the reaction front to the surface and the volume fraction of precipitate varies across the zone. More recently, a detailed analysis of internal precipitation of TiN in Ni–Ti alloys has been presented by Savva et al. [46]. The model correctly predicts the observed Ti concentration profile throughout the internal precipitation zone and allows for the calculation of the distribution of the precipitate particles. Since the terminal solubility of nitrogen in β -(Nb,Ti) is in the range 2–4 at.% at 1450°C and the transition from precipitation of TiN to precipitation of β -Nb₂N occurs for alloys containing ≥ 75 at.% Nb, the solubility product (molar fraction basis) of TiN and β -Nb₂N in Nb–Ti alloys can be estimated to be of the order of 10^{-3} . This value can be compared with the solubility product for precipitation of TiN in diluted Ni–Ti alloys: $\approx 10^{-8}$ – 10^{-9} (molar fraction basis) at 1020°C [46]. The lower solubility product in comparison to TiN precipitation in Nb–Ti, is mainly the consequence of the low solubility of nitrogen in Ni, which is of the order of a few ppm. Internal precipitation in the Nb–Ti–N system as observed in the present work differs significantly from the classical ‘Wagnerian behaviour’ but shows many features comparable to those of the previous examples: (i) the precipitating compounds possess high solubility product; (ii) the thermodynamic stability of the nitrides δ -TiN and β -Nb₂N is not very different; (iii) the activity of the precipitating element does not go to zero at the reaction front as demonstrated by the EPMA composition profiles; (iv) enlargement of the precipitates continues behind the reaction front; (v) contrary to Wagner’s assumption, the morphology of the precipitate particles is often non-spherical. Therefore, the quantitative treatment of the internal precipitation process in the Nb–Ti–N system requires an accurate modelling of the ternary diffusion problem of the type presented in Refs. [43,46], which is beyond the aim of this work. In any case, a comparison between the prediction of a model and the experimental data is not trivial because of the dearth of thermodynamic (solubility product, concentrations at the precipitation front) and diffusion data (nitrogen diffusivity in Nb–Ti alloys) for the Nb–Ti–N system.

4.4.3. The parabolic nitridation stage

The Arrhenius plot of the parabolic constants reported in Table 2 (overall nitridation kinetics) is shown in Fig. 12. The corresponding apparent activation energies are reported in Table 4. The activation energies for nitridation of the pure elements [31,47] are included for comparison. It is worth noting that the apparent activation energies do not have, in general, a precise physical meaning, as the total nitrogen uptake reflects the sum of different processes. Only when one term becomes predominant, the apparent activation energy can be compared with diffusion activa-

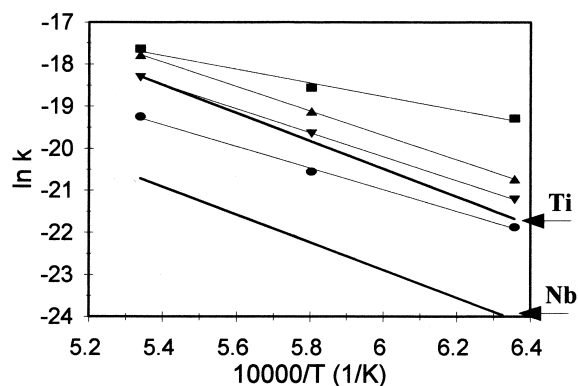


Fig. 12. Arrhenius plot of the parabolic rate constants corresponding to the weight gain kinetics measured under 0.3 bar nitrogen. (■) Ti₉₀Nb₁₀, (▲) Ti₆₃Nb₃₇, (▼) Ti₄₇Nb₅₃, (●) Ti₁₀Nb₉₀. Parabolic constants in g² cm⁻⁴ s⁻¹. The error bars are smaller than the size of the symbols.

tion energies. However, the comparison between the diffusion activation energies and the apparent activation energies obtained from the overall nitridation kinetics is complicated by the dependence of the equilibrium nitrogen concentration at the interfaces upon temperature, in particular for the α -Ti(N)– β -(Ti)(N) and the Nb(N)– β -Nb₂N equilibria. Nevertheless, the Arrhenius plot is a useful method to compare different data sets. All the alloys react faster than niobium and only Ti₁₀Nb₉₀ reacts slower than titanium. The apparent activation energies are lower than those corresponding to the pure metals and depend on the alloy composition. The activation energy of Ti₆₃Nb₃₇ and Ti₄₇Nb₅₃ is practically the same, meaning that the nitridation mechanism is very similar as can be inferred from the close microstructural evolution. The decrease of the activation energy in comparison with the pure metals is directly connected to the remarkable contribution of the internal precipitation process to the overall kinetics. In particular, for alloys Ti₆₃Nb₃₇ and Ti₄₇Nb₅₃, where the external scale is very thin, the apparent activation energy should more closely reflect the activation energy of the diffusion process which controls internal precipitation. Moreover, the data lie exceptionally well on straight lines, supporting the hypothesis of a single dominating mechanism. The observed values (237–241 kJ mol⁻¹) compare well with

Table 4

Apparent activation energies for the overall nitridation kinetics (weight gain) of Nb–Ti alloys ($p=0.3$ bar)

Alloy	Q (kJ mol ⁻¹)
Ti ^a	276
Ti ₉₀ Nb ₁₀	134±16
Ti ₆₃ Nb ₃₇	241±2
Ti ₄₇ Nb ₅₃	237±2
Ti ₁₀ Nb ₉₀	214±10
Nb ^b	274

^a1230–1500°C, $p(N_2)=1$ atm, [47].

^b1400–1900°C, $p(N_2)=0.15$ atm, [31].

the activation energy for N diffusion in Nb (235 kJ mol⁻¹ [32]) as well as with the activation energy for Nb–Ti interdiffusion (209 kJ mol⁻¹ for Ti₆₀Nb₄₀ and 239 kJ mol⁻¹ for Ti₄₀Nb₆₀ [37]). In the case of Ti₉₀Nb₁₀, the absence of a continuous α -Ti(N) layer as observed for nitridation of pure titanium can be partly responsible of the observed low activation energy (134 kJ mol⁻¹). The available literature [31–36] indicates a higher activation energy for nitrogen diffusion in α -Ti(N) (190–250 kJ mol⁻¹) in comparison to that in β -Ti(N) (140–200 kJ mol⁻¹). In addition, the activation energy for Nb–Ti interdiffusion is reported to strongly decrease as the Ti concentration increases (264 kJ mol⁻¹ for Ti₂₀Nb₈₀ and 184 kJ mol⁻¹ for Ti₈₀Nb₂₀ [37]). In the case of Ti₁₀Nb₉₀, it was possible to calculate the apparent activation energies corresponding to the layer growth kinetics (Fig. 11a–c). The resulting values (300 kJ mol⁻¹ for δ -(Nb,Ti)N and 260 kJ mol⁻¹ for β -(Nb,Ti)₂N) are comparable with those corresponding to nitridation of pure niobium (305 kJ mol⁻¹ for δ -NbN and 239 kJ mol⁻¹ for β -Nb₂N [31]). This is further evidence of the influence of internal nitridation on the overall kinetics. It is therefore concluded that the major factor determining the dependence of the overall parabolic nitridation rate on alloy composition is either the rapid decrease of nitrogen permeability moving from pure β -Ti ($C_N D_N = 7\text{--}18 \times 10^{-9}$ mol cm⁻¹ s⁻¹ at 1450°C) to pure Nb ($C_N D_N = 2\text{--}5 \times 10^{-11}$ mol cm⁻¹ s⁻¹ at 1450°C) or the strong reduction of the Nb–Ti interdiffusion coefficient as the Nb concentration increases or, even a combination of the two effects.

5. Conclusions

Nitridation of Nb–Ti alloys (10, 47, 63 and 90 at.% Ti) was studied in the temperature range 1300–1600°C under high-purity nitrogen atmosphere (0.3, 3 and 30 bar) for times ranging from 0.5 to 50 h. The experimental results lead to the following conclusions.

Formation of an external nitride layer as well as extensive internal nitride precipitation was observed. The phases present in the nitrided samples are isostructural with those of the Nb–Ti, Nb–N and Ti–N systems. The surface nitride was δ -(Ti,Nb)N in any case. Internal nitridation gives rise to different precipitate morphologies: large oriented needles for the three Ti-rich alloys, pearlite-type lamellar structures for Ti₁₀Nb₉₀ at 1300°C, small needles and approximately spherical fine particles (≈ 1 μ m) in the case of Ti₁₀Nb₉₀ at 1450 and 1600°C. The composition of the precipitate particles changes from α -(Ti,Nb)(N) for Ti₉₀Nb₁₀, to δ -(Ti,Nb)N_{1-x} for Ti₆₃Nb₃₇ and Ti₄₇Nb₅₃ and to β -(Nb,Ti)₂N for Ti₁₀Nb₉₀. The size and the spacing of the needles decreases as the Nb content increases. In any case, the precipitates are enriched in Ti in comparison to the original alloy composition.

A detailed calculation of the elastic strain energy and of

the available chemical Gibbs free energy for nucleation of α -Ti(N) in β -Ti(N) and of β -Nb₂N in Nb(N) was carried out. The chemical Gibbs free energy change is in any case small (≈ -200 J mol⁻¹ for precipitation of α -Ti(N) and ≈ -800 J mol⁻¹ for precipitation of β -Nb₂N at 10% supersaturation) and could be further lowered by the contribution of the elastic misfit strain energy. Even in the limiting case of nil strain energy, homogeneous nucleation will be very slow or even impossible as it requires very high supersaturation values (>50% for α -Ti(N) and >30% for β -Nb₂N) to lower the free energy barrier for nucleation to the critical value of 74 kT. Therefore, initial formation of nitride precipitates in the ternary system will be strongly affected by the small chemical driving force available and by the presence of residual elastic stresses related to the volume misfit. After initial nucleation, once the nitrogen flux has decreased, the growth of existing precipitate particles become the most favoured process in the three Ti-rich alloys at all temperatures. Microstructure evolution is mainly determined by the fast inward diffusion of nitrogen and the slow Nb–Ti interdiffusion in the β -(Ti,Nb) alloy. In these conditions, strong orientation relationships between precipitates and matrix are evident. In the case of β -Nb₂N precipitation at 1450 and 1600°C, heterogeneous nucleation along grain boundaries and dislocation lines is the prevailing mechanism. Important factors in determining the different behaviour are the finer alloy grain size and the higher chemical driving force available. At 1300°C, a lamellar morphology is adopted, again reflecting a nucleation difficulty.

The observed weight gain corresponds to the sum of three different terms: dissolution of nitrogen in the alloy, internal precipitation and formation of external nitride layers. Internal nitridation is the predominant term, except for Ti₉₀Nb₁₀ at 1600°C. The weight gain kinetics was invariably parabolic; a deviation from the initial rate law was observed at 1450 and 1600°C for the longer reaction times when the sample core approaches nitrogen saturation and internal nitridation slows down. The nitridation rate depends on the niobium content, because of the very strong effect of this element on nitrogen and metal diffusion. The apparent activation energy corresponding to the parabolic rate constants as obtained from the weight gain kinetics is in any case lower (134 to 241 kJ mol⁻¹) than that corresponding to nitridation of pure niobium and titanium (274 to 276 kJ mol⁻¹). The decrease of the observed activation energies reflects the importance of the internal precipitation process.

Acknowledgements

This investigation was partly supported by the Austria–Italy Bilateral Scientific and Technological Cooperation Agreement, Project 6-4B1. We are obliged to Mr. Gaggero

Giacomo for the machining of the alloy samples and to Mr. Carlo Bottino for SEM investigation.

Appendix A

Calculation of the elastic strain energy ΔG_{strain}

Microstructural observation shows only large supercritical particles, which can have a different shape in comparison to the critical nuclei. The calculation of the elastic strain energy was then carried out for some limiting cases. The general behaviour of strain energy (coherent precipitate) predicted by isotropic elastic theory [48] is that if a precipitate is elastically harder than the matrix, the shape with minimum strain energy is a sphere. However, when the aspect ratio of a needle is not very high, the corresponding strain energy is only slightly greater than that of a sphere. The same conclusions hold also for anisotropic elasticity, provided that the difference between the elastic constants of the matrix and the precipitate is large. Therefore, the following discussion is restricted to spherical and needle-like shapes as the β -(Ti,Nb) alloy is in any case softer than the nitride phases and, in addition, analytical expressions of the strain energy are available.

The elastic strain energy of an incoherent spherical precipitate B in a matrix A is given, per unit volume of precipitate by [26]

$$\Delta G_{\text{strain}}^{\text{incoh}} = \frac{3/2}{\frac{1 + \nu_A}{2E_A} + \frac{1 - 2\nu_B}{E_B}} \varepsilon^2 \quad (\text{A1})$$

where ε is the mean linear expansion of the inclusion,

$$\varepsilon = \left(\frac{V_B^0}{V_A^0} \right)^{1/3} - 1 \quad (\text{A2})$$

V_A^0 and V_B^0 , E_A and E_B , ν_A and ν_B , the molar volume in the

unstrained state, the Young's modulus and the Poisson's ratio of the matrix and the inclusion, respectively. Both the inclusion and the matrix are considered isotropic solids. For a generic ellipsoidal inclusion with semiaxes a and b , the strain energy is given by Eq. (A1) multiplied by a function $F(a/b)$. This function takes well defined values for some limiting shapes; in particular $F=3/4$ for an incompressible cylinder.

The elastic strain energy of a coherent precipitate of arbitrary shape is given, per unit volume of precipitate, by [26]

$$\Delta G_{\text{strain}}^{\text{coh}} = \frac{E}{1 - \nu} \varepsilon^2 \quad (\text{A3})$$

where the elastic constants of the precipitate and the matrix have been taken equal. For an infinite coherent needle, the strain energy is [49]

$$\Delta G_{\text{strain}}^{\text{coh}} = \left[\frac{(1 + \nu_B)^2}{\frac{1 + \nu_A}{E_A} + \frac{(1 + \nu_B)(1 - 2\nu_B)}{E_B}} + \frac{E_B}{2} \right] \varepsilon^2 \quad (\text{A4})$$

In all cases, the elastic strain energy is proportional to the square of the mean linear misfit between the matrix and the inclusion and rapidly increases as ε increases. The elastic strain energy for the formation of α -Ti(N), δ -TiN_{0.5}, δ -TiN and β -Nb₂N in β -(Ti,Nb) were calculated according to Eqs. (A1)–(A4) and the elastic constants available in the literature [37,50–52]; the results are shown in Table 5.

The molar volume of the different phases in the unstrained state were obtained from the relevant lattice parameters [53] and the experimental density of the Nb–Ti alloys. The volume misfit of the $\beta \rightarrow \alpha$ transformation was calculated for a composition corresponding to 10 at.% N in the α phase, the average nitrogen equilibrium concentration between 1300 and 1600°C, using the lattice constants reported in [47]. The values of Table 5 should be considered just as an order-of-magnitude estimate of the

Table 5

Elastic strain energy (MJ m⁻³) for formation of α -Ti(N), TiN_{0.5}, TiN and β -Nb₂N in a β -(Ti,Nb) alloy matrix. Values in brackets are in J mol⁻¹

Inclusion	Relative volume variation (%)	Linear misfit ε	$\Delta G_{\text{strain}}^{\text{incoh}}$ sphere	$\Delta G_{\text{strain}}^{\text{incoh}}$ incompressible needle	$\Delta G_{\text{strain}}^{\text{coh}}$ any shape	$\Delta G_{\text{strain}}^{\text{coh}}$ needle
α -Ti(N)	3.1	0.01	18 (200)	19 (210)	7–30 (80–340)	17 (180)
TiN _{0.5}	4.0	0.013	33 (370)	34 (380)	26–62 (290–700)	43 (490)
TiN	5.8	0.019	78 (900)	68 (780)	95–230 (1100–2600)	130 (1500)
β -Nb ₂ N	11.1	0.036	230 (5500)	200 (4800)	200–700 (5000–17 000)	390 (9300)

elastic energy. There are different sources of uncertainty which affect the calculated strain energies. The temperature dependence of the elastic constants of pure Ti and Ti alloys was measured only for temperatures up to $\approx 500^\circ\text{C}$ [37]. Regarding TiN, the available elastic data refer to room temperature [51]. As a consequence, the elastic energy was computed using the values of the elastic constants at room temperature for all phases. The effect of solid solution nitrogen on the elastic constants of α -Ti and β -(Ti,Nb) alloys is unknown even though an increase of the Young's modulus is expected; the temperature effect and the nitrogen effect should partially compensate. The elastic data of hexagonal β -Nb₂N are not known and were then approximated with those of cubic NbN [52] considering β -Nb₂N as an elastically isotropic solid. Effects related to thermal expansion were neglected in any case. The mean thermal expansion coefficients of the α -Ti, β -(Ti,Nb), TiN and δ -NbN phases between 25 and 1000°C are close to each other and lie in the range $9\text{--}10 \times 10^{-6} \text{ K}^{-1}$ [37,50,52,54]. For the coherent interface case of Eq. (A3) (particle of any shape, elastic constants of the matrix and the precipitate taken equal), two limiting values can be obtained according to the elastic constants used in the calculation: those of the matrix or those of the inclusion.

Appendix B

Calculation of the chemical Gibbs' free energy

ΔG_{chem}

According to Hillert and Staffansson [55], Othani and Hillert [56] and Jonsson [57], the phases α -Ti(N) (hexagonal), β -Ti(N) (bcc), Nb(N) (bcc) and β -Nb₂N (hexagonal) were described with an interstitial sublattice model. The formula unit of each phase can be written as $(\text{M})_1 (\text{Va}, \text{N})_c$; the metal atoms M occupy the first sublattice whereas vacancies and nitrogen atoms occupy the second sublattice. The subscript c denotes the number of interstitial sites per metal atom and is fixed by the crystallographic constraints: $c = 1/2$ for the hexagonal structure, $c = 3$ for bcc and $c = 1$ for fcc. For example, in the case of the hexagonal structure of titanium, when the second sublattice is fully occupied by vacancies the result is pure α -Ti, whereas when all the interstitial sites are filled by nitrogen, the result is the hypothetical TiN₃ compound. The expression of the Gibbs free energy given by the two sublattices model is, for one mole of formula unit,

$$G_m^\Phi = y_N {}^0G_{\text{M:N}}^\Phi + y_{\text{Va}} {}^0G_{\text{M:Va}}^\Phi + cRT(y_N \ln y_N + y_{\text{Va}} \ln y_{\text{Va}}) + {}^E G_m^\Phi \quad (\text{B1})$$

where Φ denotes the phase and $y_N = (1 - y_{\text{Va}})$ is the site

fraction of nitrogen in the second sublattice. The site fraction is related to the nitrogen mole fraction, x_N , by $y_N = x_N / c(1 - x_N)$. ${}^0G_{\text{M:N}}^\Phi$ and ${}^0G_{\text{M:Va}}^\Phi$ are the Gibbs free energy of states where all the interstitial sites are filled with nitrogen atoms or vacancies, respectively, i.e. TiN₃ and α -Ti in the above example. ${}^E G_m^\Phi$ is the excess free energy, which was computed according to the regular solution model

$${}^E G_m^\Phi = y_N y_{\text{Va}} {}^0L_{\text{M:Va,N}}^\Phi \quad (\text{B2})$$

where ${}^0L_{\text{M:Va,N}}^\Phi$ is an interaction parameter not dependent on temperature.

The thermodynamic properties of the Ti–N and the Nb–N systems required to calculate the terms ${}^0G_{\text{M:N}}^\Phi$, ${}^0G_{\text{M:Va}}^\Phi$ and ${}^E G_m^\Phi$ were taken from Refs. [57,58]. The calculation of the Gibbs free energy change for phase transformation was carried out in two steps.

1. At a given temperature the Gibbs free energy of the two phases was computed as a function of the nitrogen mol fraction x_N according to Eq. (B1) and Eq. (B2). The equilibrium composition of the two phases is obtained using the common tangent method. This fact is illustrated in Fig. 13, for the equilibrium between β -Ti(N) and α -Ti(N). The equilibrium compositions were denoted with x_β^{eq} and x_α^{eq} , respectively.
2. For a given supersaturation level (50% in Fig. 13) corresponding to the composition x_β , the tangent to the β free energy curve defines the free energy change $-PQ$ available for the initial nucleation of α phase with composition x_α^{eq} .

The results are reported in Table 6 for three different supersaturation levels: 10, 20 and 50%. The same procedure was adopted for the Nb(N) \rightarrow β -Nb₂N transformation and the results are reported in Table 7.

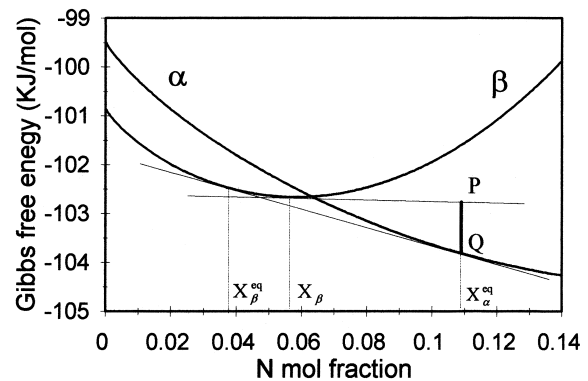


Fig. 13. Gibbs free energy curves of β -Ti(N) and α -Ti(N) solid solutions and driving force (segment PQ) corresponding to the precipitation of α -Ti with composition x_α^{eq} from a supersaturated β -Ti(N) solid solution with composition x_β .

Table 6

Chemical Gibbs free energy change (MJ m^{-3}) for nucleation of $\alpha\text{-Ti(N)}$ in $\beta\text{-Ti(N)}$. Values in brackets are in J mol^{-1} . x_{β}^{eq} is the equilibrium atomic fraction of N in $\beta\text{-Ti}$ and x_{α}^{eq} is the equilibrium atomic fraction of N in $\alpha\text{-Ti}$

Temperature (°C)	x_{β}^{eq}	x_{α}^{eq}	ΔG 10% supersat.	ΔG 20% supersat.	ΔG 50% supersat.
1300	0.0265	0.0916	−15.8 (−172)	−30.4 (−332)	−68.2 (−745)
1450	0.0374	0.1086	−22.2 (−242)	−42.7 (−466)	−95.1 (−1039)
1600	0.0485	0.1232	−28.9 (−316)	−55.4 (−605)	−121.9 (−1331)

Table 7

Chemical Gibbs free energy change (MJ m^{-3}) for nucleation of $\beta\text{-Nb}_2\text{N}$ in Nb(N) . Values in brackets are in J mol^{-1} . x_{β}^{eq} is the equilibrium atomic fraction of N in Nb and $x_{\beta\text{-Nb}_2\text{N}}^{\text{eq}}$ is the equilibrium atomic fraction of N in $\beta\text{-Nb}_2\text{N}$

Temperature (°C)	x_{β}^{eq}	$x_{\beta\text{-Nb}_2\text{N}}^{\text{eq}}$	ΔG 10% supersat.	ΔG 20% supersat.	ΔG 50% supersat.
1300	0.0139	0.3060	−32.8 (−788)	−62.4 (−1502)	−138.9 (−3341)
1450	0.0225	0.3025	−34.5 (−830)	−66.6 (−1603)	−149.4 (−3594)
1600	0.0340	0.2996	−37.6 (−905)	−71.9 (−1731)	−160.1 (−3852)

References

- [1] N. Pessall, J.K. Hulm, *Physics* 2 (1966) 311.
- [2] C.M. Yen, L.E. Toth, Y.M. Shy, D.E. Anderson, L.G. Rosner, *J. Appl. Phys.* 38 (1967) 2268.
- [3] G. Horn, E. Saur, *Z. Physik* 210 (1968) 70.
- [4] V. Buscaglia, R. Musenich, R. Parodi, W. Lengauer, W. Mayr, A. Tuissi, in: J.K. Gregory, H.J. Rack, D. Eylon (Eds.), *Surface Performance of Titanium, The Minerals, Metals and Materials Society (TMS), Warrendale, PA, 1996*, p. 75.
- [5] J.L. Murray, Assessed Nb–Ti phase diagram, in: T.B. Massalski (Ed.), *Binary Alloy Phase Diagrams, The American Society for Metals, Metals Park, OH, 1986*, p. 1699.
- [6] W. Lengauer, *Acta Metall. Mater.* 39 (1991) 2985.
- [7] H.A. Wriedt, J.L. Murray, Assessed N–Ti Phase Diagram, in: T.B. Massalski (Ed.), *Binary Alloy Phase Diagrams, The American Society for Metals, OH, Metals Park, 1986*, p. 1652.
- [8] G. Brauer, W. Kern, *Z. Anorg. Allg. Chem.* 507 (1983) 127.
- [9] C. Politis, Progress Report KfK2881, Kernforschungszentrum Karlsruhe, Germany, 1979.
- [10] M. Joguet, W. Lengauer, M. Bohn, J. Bauer, *J. Alloys Comp.*, in press.
- [11] H. Hollek, *Binäre und Ternäre-Carbid- und Nitridsysteme der Übergangsmetalle*, Gebrüder Borntraeger, Berlin, 1984.
- [12] A.A. Kodentsov, J.H. Gülpen, C. Cserhati, J.K. Kivilahti, F.J.J. Van Loo, *Metall. Mater. Trans.* 27A (1996) 59.
- [13] K. Tjokro, D.J. Young, *Oxid. Metals* 44 (1995) 453.
- [14] E.J. Felten, *J. Less-Common Met.* 17 (1969) 207.
- [15] V. Buscaglia, C. Bottino, R. Musenich, P. Fabbriatore, G. Gemme, R. Parodi, B. Zhang, P. Parodi, *J. Alloys Comp.* 226 (1995) 232.
- [16] W. Mayr, W. Lengauer, V. Buscaglia, J. Bauer, M. Bohn, M. Fialin, *J. Alloys Comp.* 262–263 (1997) 521.
- [17] W. Lengauer, *J. Alloys Comp.* 229 (1995) 80.
- [18] A. Taylor, J. Doyle, *J. Less-Common Met.* 13 (1967) 399.
- [19] O. Knacke, O. Kubaschewski, K. Hesselmann, *Thermochemical Properties of Inorganic Substances*, Springer, Berlin, 1991.
- [20] J.K. Gregory, C. Müller, U. Holzwarth, in: A. Vassel, D. Eylon, Y. Combres (Eds.), *Beta Titanium Alloys, Société Française de Métallurgie et de Matériaux, Paris, 1994*, p. 237.
- [21] C. Hu, H. Xin, L.M. Watson, T.N. Baker, *Acta Mater.* 45 (1997) 4311.
- [22] W. Lengauer, B. Tayenthal, R. Täubler, P. Ettmayer, in: *Nichtmetalle in Metallen '92, DGM Informationsgesellschaft, Verlag, Oberursel, 1992*.
- [23] A. Guillou, D. Ansel, J. Debuigne, *Scripta Mat.* 38 (1998) 981.
- [24] R.J. Hanrahan Jr., D.P. Butt, *Oxid. Metals* 47 (1997) 317.
- [25] R.J. Hanrahan Jr., D.P. Butt, *Oxid. Metals* 48 (1997) 41.
- [26] J.W. Christian, *Transformations in Metals and Alloys, Part I, Chapter 10, Pergamon, Oxford, 1981*.
- [27] P.M. Hekker, H.C.F. Rozendaal, E.J. Mittemeijer, *J. Mater. Sci.* 20 (1985) 718.
- [28] D.S. Rickerby, S. Henderson, A. Hendry, K.H. Jack, *Acta Metall.* 34 (1986) 1687.
- [29] M.H. Biglari, C.M. Brakman, M.A.J. Somers, W.G. Sloof, E.J. Mittemeijer, *Z. Metallkd.* 84 (1993) 124.
- [30] A. Deschanvres, A. Maisseu, G. Nouet, J. Vicens, *J. Less-Common Met.* 34 (1974) 237.
- [31] R. Musenich, P. Fabbriatore, G. Gemme, R. Parodi, M. Viviani, B. Zhang, V. Buscaglia, C. Bottino, *J. Alloys Comp.* 209 (1994) 319.
- [32] D. Rafaja, W. Lengauer, H. Wiesenberger, M. Joguet, *Metall. Mater. Trans.* 29A (1998) 439.
- [33] V.D. Repkin, G.V. Kurtukov, A.A. Kornilov, V.V. Bespalov, *Metalloterm. Protsesty v Khimii i Metallurgii, Russian Collection, Published Nauka, Novosibirsk, 1971*, p. 320 (*Defect Diffusion Data* 7 (1973) 219).
- [34] R.J. Wasilewski, G.L. Kehl, *J. Inst. Met.* 83 (1954–1955) 94.
- [35] V.S. Eremeev, Y.M. Ivanov, A.S. Panov, *Izv. Akad. Nauk. SSSR Met.* 4 (1969) 262.
- [36] Y.V. Levinskii et al., *Izv. Akad. Nauk. SSSR Neorg. Mater.* 4 (1968) 2068 (*Defect Diffusion Data*, 3 (1969) 343).
- [37] C.J. Smithells, E.A. Brandes (Eds.), *Metals Reference Book, Butterworths, London, 1978*.
- [38] V. Buscaglia, A. Martinelli, C. Bottino, R. Musenich, *J. Alloys Comp.*, 283 (1999).
- [39] R.E. Pawel, J.J. Campbell, *J. Electrochem. Soc.* 127 (1980) 2188.

- [40] D. Rafaja, W. Lengauer, P. Ettmayer, *Acta Mater.* 44 (1996) 4835.
- [41] C. Wagner, *Z. Elektrochem.* 63 (1959) 772.
- [42] R.A. Rapp, *Corrosion* 21 (1965) 382.
- [43] G.R. Laflamme, J.E. Morral, *Acta Metall.* 26 (1978) 1791.
- [44] D.L. Douglass, *Oxid. Metals* 44 (1995) 81.
- [45] H.-J. Christ, H. Biermann, F.C. Rizzo, H.G. Sockel, *Oxid. Metals* 32 (1989) 111.
- [46] G.C. Savva, G.C. Weatherly, J.S. Kirkaldy, *Metall. Mater. Trans.* 27A (1996) 1611.
- [47] J.-P. Bars, E. Etchessahar, J. Debuigne, *J. Less-Common Met.* 52 (1977) 51.
- [48] J.K. Lee, D.M. Barnett, H.I. Aaronson, *Met. Trans.* 8A (1977) 963.
- [49] D.M. Barnett, J.K. Lee, H.I. Aaronson, K.C. Russel, *Scr. Metall.* 8 (1974) 1447.
- [50] N.A. Waterman, M.F. Ashby (Eds.), *Elsevier Materials Selector*, vol. 2, Elsevier, London, 1991.
- [51] C. Kral, W. Lengauer, D. Rafaja, P. Ettmayer, *J. Alloys Comp.* 265 (1998) 215.
- [52] W. Lengauer, P. Ettmayer, *Monatsh. Chem.* 117 (1986) 275.
- [53] P. Villars, L.D. Calvert, *Pearson's Handbook of Crystallographic Data for Intermetallic Phases*, vol. 3, American Society for Metals, Metals Park, OH, 1985.
- [54] K. Aigner, W. Lengauer, D. Rafaja, P. Ettmayer, *J. Alloys Comp.* 215 (1994) 121.
- [55] M. Hillert, L.-I. Staffansson, *Acta Chem. Scand.* 24 (1970) 3618.
- [56] H. Ohtani, M. Hillert, *CALPHAD* 14 (1990) 289.
- [57] S. Jonsson, *Phase Relations in Quaternary Hard Materials*, Thesis, Royal Institute of Technology, Stockholm, 1993.
- [58] W. Huang, *Metall. Mater. Trans.* 27A (1996) 3591.